Electrical Power and Energy Systems 160 (2024) 110135

Contents lists available at ScienceDirect

International Journal of Electrical Power and Energy Systems

journal homepage: www.elsevier.com/locate/ijepes

Electric power-system's global-inertia estimation ☆

Angelo Maurizio Brambilla [a], Davide del Giudice [a], Daniele Linaro [a], Federico Bizzarri [a,b,*]

[a] Dipartimento di Elettronica, Informazione e Bioingegneria, Politecnico di Milano, p.zza Leonardo da Vinci, no. 32, Milano, I-20133, Italy
[b] Advanced Research Center on Electronic Systems for Information and Communication Technologies E. De Castro (ARCES), University of Bologna, Via Toffano 2/2, Bologna, I-40125, Italy

ARTICLE INFO

Keywords:
Inertia estimation
Synthetic inertia
Online estimation
Active perturbation method
System identification
Probing signal

ABSTRACT

This work presents a technique to estimate on-line the global inertia of an electric power system by exploiting the footprint of the principal frequency system dynamics. This method can estimate the inertia provided *as a whole* by synchronous machines, as well as by converter-interfaced generators controlled to emulate the behavior of the former through virtual inertia. Probing tones are injected by a grid-forming converter-interfaced generator and its virtual rotor speed is used to extrapolate its footprint. As a result, the method requires neither measuring the active power exchange of each synchronous generator nor extrapolating their rotor speeds. Since the proposed technique is entirely data driven, it does not require any model of the power system generators/prime-movers/controllers and of the interconnecting grid. The method is comprehensively tested on a modified version of the IEEE 39-BUS system and a dynamic version of the IEEE 118-BUS system, both containing grid-forming converter-interfaced generators.

1. Introduction

1.1. Motivation

Since the beginning of the century, the importance of estimating the available inertia in electrical power grids has been steadily increasing [1]. This explains the large amount of research on this topic that one can find in the scientific literature. Limited to the "Scopus" abstract and citation database of peer-reviewed papers, those including the keywords "inertia" and "power system" in their abstract spiked from only 30 in 2000 to 1200 in 2022. Even if the literature concerning this topic is vast and has been growing at a quickening pace, the problem is still open, despite the untiring work of numerous research groups. In this context, we present a reliable and efficient method for estimating online the *global inertia* available in a power system. The method belongs to the class of algorithms based on *active perturbations*, where proper probing signals [2] are used for system identification purposes [3,4].

1.2. Previous works

Methods for inertia estimation can be roughly classified into two broad categories: *(i)* algorithms triggered by an adequate disturbance (i.e., a significant event in the power system); *(ii)* methods that either use the measurements under normal operating conditions or rely on the transient response to probing signals (*active perturbations*) injected to seamlessly stimulate the power system. The approaches in the first group analyze the measurements of electrical frequency and active powers after a significant disturbance was detected [5–7]. When they are intended for online estimation, finding the exact instant the disturbance took place is of paramount importance, as misjudgments significantly affect the estimation process. An additional drawback is that these algorithms fail to provide updated inertia values on a continuous basis, as they need a triggering event [8,9]. The algorithms in the second group employ ambient measurements and need to run a system identification procedure [10–13], or rely on the knowledge of accurate real-time data [14], both potential limitations to the techniques. We refer the interested reader to [15–17] for in-depth reviews on these two approaches.

Focusing on *active perturbation* approaches, the method proposed in [18] was verified in an actual power system and resulted effective for small-scale islanded systems. In [19], a power system was probed by small active power changes through an energy storage system that did not impact the operational stability of the system. The goal was to provide the energy storage system operators with a tool to estimate

☆ The work of F. Bizzarri was partially supported by Italian MUR under the grant PRIN 2022 DCNanoSyn, CUP D53D23001500006, project code 2022SPFP9R.
* Corresponding author at: Dipartimento di Elettronica, Informazione e Bioingegneria, Politecnico di Milano, p.zza Leonardo da Vinci, no. 32, Milano, I-20133, Italy.
E-mail addresses: angelo.brambilla@polimi.it (A.M. Brambilla), davide.delguidice@polimi.it (D. del Giudice), daniele.linaro@polimi.it (D. Linaro), federico.bizzarri@polimi.it (F. Bizzarri).

https://doi.org/10.1016/j.ijepes.2024.110135
Received 3 November 2023; Received in revised form 22 May 2024; Accepted 8 July 2024
Available online 24 July 2024

the unknown time-varying inertia of any generic power system and properly tune/control their devices for fast-frequency strategies. Low-level probing signals were used also in [20] for accurate estimation of inertia and damping constants in microgrids by using a moving horizon estimation approach. The method proposed in [21] is possibly the most well-known in the considered class. The authors proposed a closed-loop identification technique to estimate the equivalent inertia constant at the connection bus. The method aims at estimating the inertia constant of a single device connected to the grid.

The main source of inspiration for our work was the realm of frequency synchronization of power generators. This is a necessary condition for the operation of power-grids. During steady-state operation, the frequency is the same throughout the entire power grid and any pair of generators has a fixed phase difference that determines the power flow. Even if the focus of our work is not synchronization but global inertia estimation, the main results we propose are grounded in this concept. It is thus worthwhile mentioning that one can find in the literature many contributions on synchronization (see for instance [22–28]).

1.3. Contribution

We provide a theoretical framework for the inertia estimation of an entire power system based on the dynamic response of its model containing synchronous generators equipped with primary frequency control and grid-forming (GF) converter-interfaced generators (CIGs) [29]. By interpreting the power system as a power-controlled oscillator whose instantaneous frequency is controlled by the power flows, we derive the analytical expression in the frequency domain of the *principal frequency system dynamics*. We show that this expression represents the behavior shared by the rotor speed of all the synchronous generators and also by GF CIG elements present in the grid, provided that a proper amount of *synchronization* (at low frequencies) is guaranteed among these devices. Global inertia is one of the parameters of this expression, which can thus be estimated with appropriate identification techniques. We show that the estimation depends neither on the electrical characteristics of the interconnecting lines, nor on the number of buses, controllers, governors, and synchronous machine models but only on the collected data, i.e., the proposed estimation method is agnostic with respect to the system.

Based on these considerations, we exploit a GF CIG that is either already present in the power system, or can be inserted with the specific purpose of allowing the estimation of the power system global inertia. The probing signals used to stimulate the power system in a suitable frequency band are injected by the GF CIG and its virtual rotor speed is sampled. By resorting to the vector fitting (VF) technique [30–32], we obtain the parameters that provide the best fit of the analytical expression of the frequency spectrum of the collected samples. The global inertia of the power system is among these parameters.

2. The power system as a power-controlled oscillator

In electronics, a voltage-controlled oscillator is an oscillator whose frequency is controlled by an input voltage: the applied voltage determines the instantaneous oscillation frequency. Analogously, a generic power system can be viewed as a power-controlled oscillator whose instantaneous frequency, i.e., rotor speed of synchronous generators, is controlled by the power flows.

In an oscillator, steady-state periodic solutions lack a phase reference [33,34]. Even if a limit cycle is unique and isolated in the phase space, two orbits originating from two different initial conditions belonging to this limit cycle will remain shifted in the time domain. This property is at the origin of phase noise in oscillators [35]. From the viewpoint of dynamical systems, according to Floquet's theory, this is justified by the presence of a characteristic multiplier equal to 1.

The same holds in power systems where a stationary solution is not an *isolated equilibrium* but is embedded in a *continuum of equilibria* [36]. When the power system is modeled in the dq-frame, the presence of a characteristic multiplier equal to 1 corresponds to an eigenvalue equal to 0 in the Jacobian matrix of the power system model linearized around an equilibrium point [37]. Indeed, the classical power system model aims at representing the envelope of the *actual* system dynamics through a steady-state solution. In other words, the *periodic steady-state solution* at the fundamental frequency with a *constant* envelope is actually represented as a *constant* steady-state solution playing the role of a *stationary solution* in the dq-frame.

In reality, the power system model is more complex than a voltage-controlled oscillator since it is made up of several power-controlled oscillators (viz., synchronous generators and GF CIGs) [22,27]. An overall instantaneous oscillation frequency, shared by all of these components, is observed only when these local and interconnected oscillators are synchronized. In practice, even in normal operating conditions, it never occurs but *on average*. As a matter of fact, the power system model never works at steady state because of random fluctuations in the power consumption of the loads or in the energy production of renewable energy sources.

To clarify these concepts, it is useful to discuss what happens in a power system model including N synchronous generators whose dynamic evolution is modeled by the simple swing equation[1] and that are equipped with primary frequency control. Generators are interconnected by lines and transformers, and constant-power and/or constant-impedance loads are connected to the grid buses. Under these assumptions, the overall power system model is described by the following set of $3N$ ordinary differential equations (ODEs),

$$\begin{aligned} \dot{\boldsymbol{\delta}} &= \Omega\left(\boldsymbol{\omega}-\omega_0\right) \\ \boldsymbol{\mathcal{M}}\dot{\boldsymbol{\omega}} &= \boldsymbol{P}_m - \boldsymbol{P}_e(\boldsymbol{\delta}) - \boldsymbol{\mathcal{D}}(\boldsymbol{\omega}-\omega_0) \\ \boldsymbol{T}_g\dot{\boldsymbol{P}}_m &= \boldsymbol{P}_{m_{\text{eq}}} - \boldsymbol{P}_m - \boldsymbol{k}_g\boldsymbol{R}^{-1}(\boldsymbol{\omega}-\omega_0)\,, \end{aligned} \tag{1}$$

where the meaning of the symbols in (1) is as follows[2]:

- Ω: the base synchronous frequency in rad/s;
- $\boldsymbol{\omega}(t)\in\mathbb{R}^N$: the per-unit (pu) rotor speeds of the machines;
- $\omega_0\in\mathbb{R}$: the pu reference synchronous frequency;
- $\boldsymbol{\delta}(t)\in\mathbb{R}^N$: the rotor angles of the machines;
- $\boldsymbol{\mathcal{M}}\in\mathbb{R}^{N\times N}$: a diagonal matrix whose jth element is twice the product of the inertia constant H_j[s] and the pu rated power S_{B_j} of the jth machine: $\mathcal{M}_{jj}=2H_jS_{B_j}$ for $j=1,\dots,N$. The *global inertia* of an electrical power system is given by $\mathcal{G}_M=\sum_{j=1}^{N}\mathcal{M}_{jj}=\mathbb{1}_{1,N}\boldsymbol{\mathcal{M}}\mathbb{1}_{N,1}$ and is expressed in seconds.[3]
- $\boldsymbol{\mathcal{D}}\in\mathbb{R}^{N\times N}$: a diagonal matrix whose jth element is the product of the load damping factor D_j and the pu rated power S_{B_j} of the jth machine: $\mathcal{D}_{jj}=D_jS_{B_j}$ for $j=1,\dots,N$;
- $\boldsymbol{P}_e(\boldsymbol{\delta})\in\mathbb{R}^N$: the pu electrical active power exchanged by the machines. A feature of interest of $\boldsymbol{P}_e(\boldsymbol{\delta})$ is that, given a common shift of the $\boldsymbol{\delta}$ rotor angles written as $\boldsymbol{\delta}(t)+\alpha(t)$ (where $\alpha(t)$ is a scalar function), the machines react so that $\boldsymbol{P}_e(\boldsymbol{\delta}(t)+\alpha(t))=\boldsymbol{P}_e(\boldsymbol{\delta}(t))$. In other words, power flows are only influenced by the difference among rotor angles, and not their individual values *per se*.
- $\boldsymbol{P}_m\in\mathbb{R}^N$: the pu mechanical power of the machines, governed by their prime mover;
- $\boldsymbol{P}_{m_{\text{eq}}}\in\mathbb{R}^N$: the pu mechanical power setpoint of the machines corresponding to the power flow solution;

[1] In this work, as done in [29], we model GF CIG by resorting to the swing equation (see Section 5.1). Hence, the extension to the case in which GF CIGs are present is straightforward.

[2] The last two equations in (1) are derived introducing a proper power-base quantity S_{base} shared by the overall power system.

[3] In the following $\mathbb{1}_k$ is the $k\times k$ identity matrix, $\mathbb{0}_k$ is a $k\times k$ matrix of zero elements, and $\mathbb{1}_{k,h}$ and $\mathbb{0}_{k,h}$ are $k\times h$ matrices of 1 or 0, respectively.

– $\boldsymbol{T}_g$, $\boldsymbol{k}_g$, $\boldsymbol{R} \in \mathbb{R}^{N\times N}$: diagonal matrices whose elements model the time constant, gain constant, and droop gain of the primary frequency controls, respectively.[4]

It is worth noticing that the first set of N ODEs in (1) should be written as $\dot{\boldsymbol{\delta}} = \Omega\boldsymbol{\omega}$ if one wanted to completely retain the formulation in polar coordinates of the synchronous-generator dynamical equations, in which the rotor angle grows unbounded since the rotor keeps rotating. Nevertheless, (1) is usually adopted to identify an equilibrium point of the system, say $[\boldsymbol{\delta}_{\text{eq}}^{\text{T}}, \boldsymbol{\omega}_{\text{eq}}^{\text{T}}, \boldsymbol{P}_{m_{\text{eq}}}^{\text{T}}]^{\text{T}}$, neglecting the common shifting evolution of the $\boldsymbol{\delta}$ rotor angles.

By considering the linearization of (1), we have

$$\begin{bmatrix} \Delta\dot{\boldsymbol{\delta}} \\ \Delta\dot{\boldsymbol{\omega}} \\ \Delta\dot{\boldsymbol{P}}_m \end{bmatrix} = \underbrace{\begin{bmatrix} \mathbb{O}_N & \Omega\mathbb{1}_N & \mathbb{O}_N \\ -\boldsymbol{\mathcal{M}}^{-1}\boldsymbol{\Pi} & -\boldsymbol{\mathcal{M}}^{-1}\boldsymbol{\mathcal{D}} & \boldsymbol{\mathcal{M}}^{-1} \\ \mathbb{O}_N & -\boldsymbol{T}_g^{-1}\boldsymbol{k}_g\boldsymbol{R}^{-1} & -\boldsymbol{T}_g^{-1} \end{bmatrix}}_{\boldsymbol{A}} \begin{bmatrix} \Delta\boldsymbol{\delta} \\ \Delta\boldsymbol{\omega} \\ \Delta\boldsymbol{P}_m \end{bmatrix}, \tag{2}$$

where the $\boldsymbol{\Pi} = {}^{\partial \boldsymbol{P}_e}/_{\partial\boldsymbol{\delta}}$ matrix is the grid interconnection Laplacian *singular* matrix [38] and $\boldsymbol{\Pi} = \boldsymbol{\Pi}^{\text{T}}$. The null space of $\boldsymbol{\Pi}$ is spanned by $\ker(\boldsymbol{\Pi}) = \mathbb{1}_{N,1}$. The $\boldsymbol{A}$ matrix is thus singular too and $\ker(\boldsymbol{A}) \equiv \boldsymbol{u}_1 = [\mathbb{1}_{1,N}, \mathbb{O}_{1,2N}]^{\text{T}}$.

When a small signal $\boldsymbol{b}(t) \in \mathbb{R}^N$ is added to $\boldsymbol{P}_e(\boldsymbol{\delta}(t))$, thus emulating the injection of (stochastic) disturbances or probing signals, the N ODEs in (1) governing $\dot{\boldsymbol{\omega}}$ become

$$\boldsymbol{\mathcal{M}}\dot{\boldsymbol{\omega}} = \boldsymbol{P}_m - \boldsymbol{P}_e(\boldsymbol{\delta}) - \boldsymbol{\mathcal{D}}(\boldsymbol{\omega} - \omega_0) + \boldsymbol{b}(t) \ . \tag{3}$$

Since $\boldsymbol{A}$ is singular, it is not possible to exploit (2) to obtain an approximate solution of (3) in the neighborhood of $[\boldsymbol{\delta}_{\text{eq}}^{\text{T}}, \boldsymbol{\omega}_{\text{eq}}^{\text{T}}, \boldsymbol{P}_{m_{\text{eq}}}^{\text{T}}]^{\text{T}}$. Nevertheless, in this case, the singularity of $\boldsymbol{\Pi}$ is a key aspect to allow resorting to the small-signal formulation to study the perturbed evolution of $\boldsymbol{\omega}(t) = \boldsymbol{\omega}_{\text{eq}} + \Delta\boldsymbol{\omega}(t)$. To explore this aspect, let us define $\boldsymbol{u}_k$ and $\boldsymbol{v}_k$ as the $3N$ right and left eigenvectors of $\boldsymbol{A}$, respectively ($\boldsymbol{u}_1$ and $\boldsymbol{v}_1$ are associated to the $\lambda_1 = 0$ eigenvalue). So doing we are assuming that $\boldsymbol{A}$ has distinct eigenvalues (their values are related to the eigenvalues of $\boldsymbol{\Pi}$ [38] and to the primary frequency control time constants) and is diagonalizable.

Because of the bi-orthogonality property of eigenvectors (i.e., $\boldsymbol{v}_k^{\text{T}}\boldsymbol{u}_j \neq 0$ only if $k \neq j$), it is always possible to write[5]

$$\begin{bmatrix} \mathbb{O}_{N,1} \\ \boldsymbol{\mathcal{M}}^{-1}\boldsymbol{b}(t) \\ \mathbb{O}_{N,1} \end{bmatrix} = \underbrace{\boldsymbol{v}_1^{\text{T}} \begin{bmatrix} \mathbb{O}_{N,1} \\ \boldsymbol{\mathcal{M}}^{-1}\boldsymbol{b}(t) \\ \mathbb{O}_{N,1} \end{bmatrix} \boldsymbol{u}_1}_{\boldsymbol{b}_\delta(t)} + \underbrace{\sum_{k=2}^{3N} \boldsymbol{v}_k^{\text{T}} \begin{bmatrix} \mathbb{O}_{N,1} \\ \boldsymbol{\mathcal{M}}^{-1}\boldsymbol{b}(t) \\ \mathbb{O}_{N,1} \end{bmatrix} \boldsymbol{u}_k}_{\boldsymbol{b}_{\delta\omega}(t)} . \tag{4}$$

Since, as derived in Appendix A,

$$\boldsymbol{v}_1 = \ker(\boldsymbol{A}^{\text{T}}) = \frac{\Omega}{\mathbb{1}_{1,N}\boldsymbol{\Theta}\mathbb{1}_{N,1}} \begin{bmatrix} \mathbb{1}_{N,1}\boldsymbol{\Theta}\Omega^{-1} \\ \boldsymbol{\mathcal{M}}\mathbb{1}_{N,1} \\ \boldsymbol{T}_g\mathbb{1}_{N,1} \end{bmatrix}, \tag{5}$$

one obtains

$$\boldsymbol{b}_\delta(t) = \frac{\Omega}{\mathbb{1}_{1,N}\boldsymbol{\Theta}\mathbb{1}_{N,1}} \begin{bmatrix} \mathbb{1}_{1,N}\boldsymbol{b}(t)\mathbb{1}_{N,1} \\ \mathbb{O}_{2N,1} \end{bmatrix}, \tag{6}$$

and

$$\boldsymbol{b}_{\delta\omega}(t) = \begin{bmatrix} -\Omega\frac{\mathbb{1}_{1,N}\boldsymbol{b}(t)\mathbb{1}_{N,1}}{\mathbb{1}_{1,N}\boldsymbol{\Theta}\mathbb{1}_{N,1}} \\ \boldsymbol{\mathcal{M}}^{-1}\boldsymbol{b}(t) \\ \mathbb{O}_{N,1} \end{bmatrix}, \tag{7}$$

where $\boldsymbol{\Theta} = \boldsymbol{\mathcal{D}} + \boldsymbol{k}_g\boldsymbol{R}^{-1}$.

[4] For the sake of simplicity, we assume that all the N synchronous generators are equipped with primary frequency control. The less generic case in which only a subset of them shares this property can be straightforwardly formalized.

[5] In general, for $k = 1 \dots 3N$, $\boldsymbol{v}_k^{\text{T}}\boldsymbol{u}_k \neq 1$ but it is always possible to scale each $\boldsymbol{v}_k$ w.r.t. $\boldsymbol{v}_k^{\text{T}}\boldsymbol{u}_k$, thus obtaining a new vector $\hat{\boldsymbol{v}}_k$ such that $\hat{\boldsymbol{v}}_k^{\text{T}}\boldsymbol{u}_k = 1$. This is done in the following but omitting the $\hat{}$ symbol to keep notation terse.

The effect of $\boldsymbol{b}_\delta(t)$ is thus to *synchronously* shift all the components of $\boldsymbol{\delta}$ of the same time-varying quantity

$$\alpha(t) = \Omega\int_0^t \frac{\mathbb{1}_{1,N}\boldsymbol{b}(\tau)}{\mathbb{1}_{1,N}\boldsymbol{\Theta}\mathbb{1}_{N,1}} d\tau \ , \tag{8}$$

without altering the $\boldsymbol{\omega}(t)$ vector since $\boldsymbol{P}_e(\boldsymbol{\delta}(t) + \alpha(t)) = \boldsymbol{P}_e(\boldsymbol{\delta}(t))$. If $\mathbb{1}_{1,N}\boldsymbol{b}(\tau)$ has a nonzero mean value $\alpha(t)$, would increase unbounded. This would be true even if $\boldsymbol{b}(\tau)$ were a vector of random variables with zero mean and finite variance as the Ornstein-Uhlenbeck (OU) processes typically used to model stochastic variability of power loads [39–42]. As a matter of fact, $\alpha(t)$ would exhibit unbounded variance [43] and thus *the effect of $\boldsymbol{b}_\delta(t)$ cannot be treated as that of a small signal, even being $\boldsymbol{b}_\delta(t)$ actually small*. In the literature, this is known as phase noise [35].

On the contrary, it is possible to compute the effect of $\boldsymbol{b}_{\delta\omega}(t)$ by resorting to the small-signal approach since it is easy to verify that $\boldsymbol{v}_1^{\text{T}}\boldsymbol{b}_{\delta\omega}(t)\boldsymbol{u}_1 = 0$. This implies that $\boldsymbol{b}_{\delta\omega}(t)$ does not produce any effect similar to $\alpha(t)$. That is, it is not responsible for coherent phase shifting in the entire power system but produces small fluctuations that are different for all the components of $\boldsymbol{\delta}(t)$. The main implication of this result is that, in the presence of a small signal $\boldsymbol{b}_{\delta\omega}(t)$, *the power system does not remain synchronized*. In other words, it is possible to prove that, in the presence of the small signal $\boldsymbol{b}_{\delta\omega}(t)$, the assumption that the power system remains synchronized, viz. $\Delta\omega_k(t) \equiv \Delta\omega(t)$ for $k = 1, \dots, N$ (or, equivalently, $\Delta\boldsymbol{\omega}(t) = \Delta\omega(t)\mathbb{1}_{N,1}$) is inconsistent with the equations governing the power system itself. This can be derived by focusing on the ODEs governing the dynamics of $\Delta\boldsymbol{\omega}$. We can write

$$\begin{aligned} \boldsymbol{\mathcal{M}}\Delta\dot{\boldsymbol{\omega}} &= \Delta\boldsymbol{P}_m - \boldsymbol{\Pi}(\alpha(t)\mathbb{1}_{N,1} + \Delta\boldsymbol{\delta}(t)) - \boldsymbol{\mathcal{D}}\Delta\boldsymbol{\omega} + \boldsymbol{b}(t) \\ &= \Delta\boldsymbol{P}_m - \boldsymbol{\Pi}\Delta\boldsymbol{\delta}(t) - \boldsymbol{\mathcal{D}}\Delta\boldsymbol{\omega} + \boldsymbol{b}(t) \\ &= \Delta\boldsymbol{P}_m - \boldsymbol{\Pi}\int\Omega\Delta\boldsymbol{\omega}(t)dt - \boldsymbol{\mathcal{D}}\Delta\boldsymbol{\omega} + \boldsymbol{b}(t) \ , \end{aligned} \tag{9}$$

with $\Delta\boldsymbol{\omega}$ evolving in the neighborhood of $\boldsymbol{\omega}_{\text{eq}}$, i.e., of the frequency at the equilibrium point. It is worth noticing that, thanks to the singularity of $\boldsymbol{\Pi}$, the possibly unbounded contribution of $\alpha(t)\mathbb{1}_{N,1}$ does not affect $\Delta\dot{\boldsymbol{\omega}}$.

Assuming $\Delta\boldsymbol{\omega}(t) = \Delta\omega(t)\mathbb{1}_{N,1}$, $\Delta\omega(0) = 0$, and $\Delta\boldsymbol{P}_m(0) = \mathbb{O}_{N,1}$, Eq. (9) can be transformed in the s-domain as

$$\begin{aligned} s\Delta\omega(s)\boldsymbol{\mathcal{M}}\mathbb{1}_{N,1} &= \Delta\boldsymbol{P}_m(s) - \Omega\frac{\Delta\omega(s)}{s}\underbrace{\boldsymbol{\Pi}\mathbb{1}_{N,1}}_{\mathbb{O}_{N,1}} - \Delta\omega(s)\boldsymbol{\mathcal{D}}\mathbb{1}_{N,1} + \boldsymbol{b}(s) \\ &= \Delta\boldsymbol{P}_m(s) - \Delta\omega(s)\boldsymbol{\mathcal{D}}\mathbb{1}_{N,1} + \boldsymbol{b}(s) \ . \end{aligned}$$

Since $\Delta\boldsymbol{P}_m(s) = -\left(s\boldsymbol{T}_g + \mathbb{1}_N\right)^{-1}\boldsymbol{k}_g\boldsymbol{R}^{-1}\mathbb{1}_{N,1}\Delta\omega(s)$, we obtain

$$\boldsymbol{\Xi}\mathbb{1}_{N,1}\Delta\omega(s) = \boldsymbol{b}(s) \ , \tag{10}$$

where $\boldsymbol{\Xi} = s\boldsymbol{\mathcal{M}} + \boldsymbol{\mathcal{D}} + \left(s\boldsymbol{T}_g + \mathbb{1}_N\right)^{-1}\boldsymbol{k}_g\boldsymbol{R}^{-1}$. It is worth noting that the above equality is not verified in general. Indeed, $\boldsymbol{\Xi}$ is a diagonal matrix that generically does not contain identical elements in its diagonal, while the right-hand side of Eq. (10) leads to a column vector of possibly different elements. As a consequence, it is not possible to *generally* ensure that $\Delta\boldsymbol{\omega}(t) = \Delta\omega(t)\mathbb{1}_{N,1}$, thus *violating the initial hypothesis that generators remain synchronized in the presence of a small signal $\boldsymbol{b}_{\delta\omega}(t)$*.

How is it possible to reconcile this result with the well-known experimental evidence that, in properly connected power systems, the components of $\Delta\boldsymbol{\omega}(t)$ share almost the same spectrum at low frequency?[6]

To answer this question, let us consider the small perturbation of the so-called *principal frequency system dynamics*, viz. the frequency that can be defined for the center of inertia (COI) of the system [44], i.e.,

$$\Delta\omega_{\text{COI}}(t) = \frac{\sum_{k=1}^N S_{B_k}H_k\Delta\omega_k(t)}{\sum_{k=1}^N S_{B_k}H_k} \ , \tag{11}$$

which can also be recast as

$$\mathcal{G}_{\mathcal{M}}\Delta\omega_{\text{COI}}(t) = \mathbb{1}_{1,N}\boldsymbol{\mathcal{M}}\Delta\boldsymbol{\omega}(t), \tag{12}$$

[6] The interested reader can find in Appendix B an exemplification of this statement.

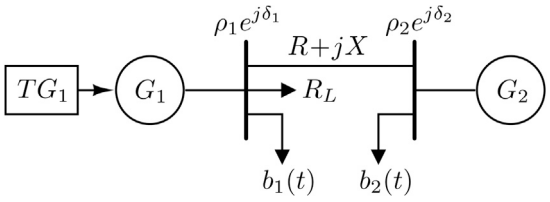

Fig. 1. The schematic of the power test system. R_L is a resistive load, $b_1(t)$ and $b_2(t)$ are small-signal (stochastic) perturbations that vary the active power absorbed by the grid at the power flow solution and which are neglected in the large-signal model of the power system. For the sake of simplicity, the internal impedance of both G_1 and G_2 is assumed to be zero, and only the G_1 generator is equipped with a turbine governor.

where $\mathcal{G}_{\mathcal{M}} = \mathbb{1}_{1,N}\boldsymbol{\mathcal{M}}\mathbb{1}_{N,1}$ is the power system global inertia already defined in the previous section. The ODE governing the evolution of $\Delta\omega_{\text{COI}}(t)$ is

$$\begin{aligned}\mathcal{G}_{\mathcal{M}}\Delta\dot{\omega}_{\text{COI}}(t) &= \mathbb{1}_{1,N}\boldsymbol{\mathcal{M}}\Delta\dot{\boldsymbol{\omega}}(t)\\ &= \mathbb{1}_{1,N}\left(\Delta\boldsymbol{P}_m - \Delta\boldsymbol{P}_e - \boldsymbol{\mathcal{D}}\Delta\boldsymbol{\omega} + \boldsymbol{b}(t)\right)\ .\end{aligned} \tag{13}$$

If we write $\boldsymbol{b} = \boldsymbol{b}^{\text{lf}} + \boldsymbol{b}^{\text{hf}}$, where $^{\text{lf}}$ and $^{\text{hf}}$ stand for low- and high-frequency, respectively, and $\boldsymbol{b}^{\text{lf}}$ is assumed to generate $\Delta\boldsymbol{\omega}(t) \approx \Delta\omega(t)\mathbb{1}_{N,1}$, we obtain $\Delta\omega_{\text{COI}}(t) \approx \Delta\omega(t)$. Based on the properties derived so far, it is possible to express the dynamics of $\Delta\omega(t)$ in the Laplace domain at low frequency as

$$\Delta\omega(s) = \frac{\mathbb{1}_{1,N}\boldsymbol{b}^{\text{lf}}(s)}{s\mathcal{G}_{\mathcal{M}} + \mathbb{1}_{1,N}\left(\boldsymbol{\mathcal{D}} + \left(s\boldsymbol{T}_g + \mathbb{1}_N\right)^{-1}\boldsymbol{k}_g\boldsymbol{R}^{-1}\right)\mathbb{1}_{N,1}}\ . \tag{14}$$

In particular, Eq. (14) provides the expression of the frequency spectrum almost shared by all the $\Delta\omega_k(t)$ variables at low frequency.

As it is shown in Appendix C, by assuming that each of the $\widetilde{N} \le N$ primary frequency-controller block is characterized by a different time constant, the denominator of (14) is an $(\widetilde{N}+1)$-order polynomial in the s variable, hence (14) can be recast as

$$\Delta\omega(s) = \eta(s)\sum_{k=1}^{\widetilde{N}+1}\frac{c_k}{s-a_k}\ ,$$

where a_k $(k = 1,\dots\widetilde{N}+1)$ are the poles, c_k $(k = 1,\dots\widetilde{N}+1)$ are the residues, and $\eta(s) = \mathbb{1}_{1,N}\boldsymbol{b}^{\text{lf}}(s)$. Furthermore, it can be derived that $\mathcal{G}_{\mathcal{M}}^{-1} = \sum_{k=1}^{\widetilde{N}+1} c_k$.

3. Global inertia estimation: an insight

Our aim is exploiting (14) to systematically derive the global inertia $\mathcal{G}_{\mathcal{M}}$ of a given power system. To give an example-driven insight into the approach we are proposing, we present a simple case-study whose first goal is to show how Eq. (14) can be derived.

3.1. Low-frequency characterization

The large-signal model of the system in Fig. 1, in which the $b_1(t)$ and $b_2(t)$ small-signals are neglected, is given by the following equations:

$$\begin{aligned}\dot{\delta}_1 &= \Omega\left(\omega_1 - \omega_0\right)\\ \dot{\delta}_2 &= \Omega\left(\omega_2 - \omega_0\right)\\ \mathcal{M}_1\dot{\omega}_1 &= P_{m_1} - P_{e_1}(\delta_1,\delta_2) - \mathcal{D}_1\left(\omega_1 - \omega_0\right)\ ,\\ \mathcal{M}_2\dot{\omega}_2 &= P_{m_2} - P_{e_2}(\delta_1,\delta_2) - \mathcal{D}_2\left(\omega_2 - \omega_0\right)\\ T_{g_1}\dot{P}_{m_1} &= P_{m_{\text{eq}_1}} - P_{m_1} - k_{g_1}R_1^{-1}\left(\omega_1 - \omega_0\right)\end{aligned} \tag{15}$$

where

$$P_{e_1}(\delta_1,\delta_2) = \frac{1}{R^2+X^2}\left[R\rho_1^2 - R\rho_1\rho_2\cos(\delta_1-\delta_2) + X\rho_1\rho_2\sin(\delta_1-\delta_2)\right]\frac{\rho_1^2}{R_L}\ ,$$

and

$$P_{e_2}(\delta_1,\delta_2) = \frac{1}{R^2+X^2}\left[R\rho_2^2 - R\rho_1\rho_2\cos(\delta_2-\delta_1) + X\rho_1\rho_2\sin(\delta_2-\delta_1)\right]\ .$$

Table 1
Parameters for the case study in Fig. 1.

S_{B_1}	1 pu	S_{B_2}	1 pu	V_{base}	100 kV
D_1	1	D_2	1	Z_{base}	100 Ω
H_1	4 s	H_2	2.5 s	R_L	$^{10}/_{9}$ pu
T_{g_1}	50 s	$k_{g_1}R_1^{-1}$	50	$R=X$	10^{-3} pu
$P_{m_{\text{eq}_1}}$	0.4 pu	$P_{m_{\text{eq}_2}}$	0.6 pu	S_{base}	100 MVA

The last equation in (15) models the turbine governor connected to the G_1 generator.[7] The power system is assumed to be at steady state, with $\omega_k = \omega_{\text{eq}_k} = \omega_0 = 1$, $\delta_k = \delta_{\text{eq}_k}$, and $P_{m_k} = P_{m_{\text{eq}_k}} = P_{e_k}(\delta_{\text{eq}_1},\delta_{\text{eq}_2})$ for $k \in \{1,2\}$. The small-signal equivalent model of (15), including now the small-signal additive perturbations projected according to (4), is

$$\begin{aligned}\Delta\dot{\delta}_1 &= \Omega\Delta\omega_1\\ \Delta\dot{\delta}_2 &= \Omega\Delta\omega_2\\ \mathcal{M}_1\Delta\dot{\omega}_1 &= \xi(\Delta\delta_2 - \Delta\delta_1) - \mathcal{D}_1\Delta\omega_1 + \Delta P_{m_1} + b_1(t)\\ \mathcal{M}_2\Delta\dot{\omega}_2 &= \nu\xi(\Delta\delta_1 - \Delta\delta_2) - \mathcal{D}_2\Delta\omega_2 + b_2(t)\\ T_{g_1}\Delta\dot{P}_{m_1} &= -\Delta P_{m_1} - k_{g_1}R_1^{-1}\Delta\omega_1\end{aligned} \tag{16}$$

where

$$\xi = \frac{\rho_1\rho_2}{R^2+X^2}\left(R\sin(\delta_{\text{eq}_1}-\delta_{\text{eq}_2}) + X\cos(\delta_{\text{eq}_1}-\delta_{\text{eq}_2})\right)\ ,$$

and

$$\nu = \frac{1-\frac{R}{X}\tan(\delta_{\text{eq}_1}-\delta_{\text{eq}_2})}{1+\frac{R}{X}\tan(\delta_{\text{eq}_1}-\delta_{\text{eq}_2})}\ .$$

By transforming (16) in the Laplace domain, the $\Delta\omega_1(s)$ and $\Delta\omega_2(s)$ small-signal variations of the rotor speeds of the two synchronous generators can be written as

$$\begin{aligned}\Delta\omega_1(s) &= \frac{\beta_3^1(s)s^3 + \beta_2^1(s)s^2 + \beta_1^1(s)s + \beta_0^1(s)}{\alpha_4 s^4 + \alpha_3 s^3 + \alpha_2 s^2 + \alpha_1 s + \alpha_0}\\ \Delta\omega_2(s) &= \frac{\beta_3^2(s)s^3 + \beta_2^2(s)s^2 + \beta_1^2(s)s + \beta_0^2(s)}{\alpha_4 s^4 + \alpha_3 s^3 + \alpha_2 s^2 + \alpha_1 s + \alpha_0}\end{aligned}\ , \tag{17}$$

where the α_k and β_k^j coefficients are reported in Appendix D. For *sufficiently small* values of s (i.e., at low frequency), in (17) we can neglect $\alpha_k s^k$ for $k \in \{3,4\}$ and $\beta_k^j s^k$ for $k \in \{2,3\}$, $j \in \{1,2\}$. Furthermore, in the coefficients reported in Appendix D we neglect all the terms divided by $\xi\Omega$, since we assume $\xi\Omega \gg 1$ and $\nu \approx 1$. So doing, both $\Delta\omega_1(s)$ and $\Delta\omega_2(s)$ reduce to

$$\begin{aligned}&\Delta\omega(s)\\ &= \frac{(sT_{g_1}+1)(b_1^{\text{lf}}(s)+b_2^{\text{lf}}(s))}{s^2(\mathcal{M}_1+\mathcal{M}_2)T_{g_1} + s\left((\mathcal{D}_1+\mathcal{D}_2)T_{g_1} + \mathcal{M}_1+\mathcal{M}_2\right) + \left((\mathcal{D}_1+\mathcal{D}_2) + k_{g_1}R_1^{-1}\right)}\ .\end{aligned} \tag{18}$$

The same expression can be derived from the most generic one in (14).

Fig. 2 shows the plots corresponding to the (17) and (18) expressions. As it can be noticed, the approximation is extremely good for $f < 10$ Hz. The expressions of $\Delta\omega_1(s)$ and $\Delta\omega_2(s)$ at low frequencies turn out to be *identical*; this means that the $\Delta\delta_1$ and $\Delta\delta_2$ corresponding angles vary in a synchronized way.

[7] We modeled turbine governors with a dominant pole transfer function, as done for example in [22]. Some turbine governors may require a more complex transfer function consisting of a zero and a pair of higher frequency poles. To keep notation simple, we adopted in this example the former modeling. Nonetheless, the proposed methodology is compatible with any governor model.

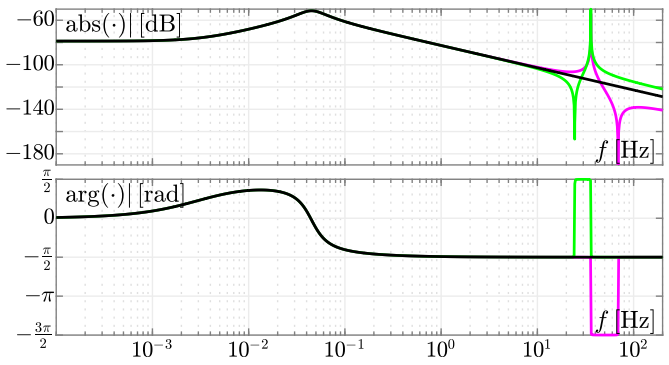

Fig. 2. The modulus and the phase of $\Delta\omega_1$ (in magenta, see (17)), $\Delta\omega_2$ (in green, see (17)), and $\Delta\omega$ (in black, see (18)) are shown in the upper and lower panel, respectively. These curves are derived for the power system in Fig. 1 with $\nu = 1.002$ and by assuming the parameters' value reported in Table 1. $b_1(t)$ and $b_2(t)$ are sinusoidal functions whose phase is zero and whose amplitude is fixed at 100 kW and 500 kW, respectively, for each value of f.

3.2. Global inertia estimation

As we did for (14), since in this case $\widetilde{N} = 1$, we can recast (18) as

$$\begin{aligned}\Delta\omega(s) &= \left(\frac{c_1}{s-a_1} + \frac{c_2}{s-a_2}\right)\eta(s)\\ &= \frac{(c_1+c_2)s - c_1a_2 - c_2a_1}{s^2 - s(a_1+a_2) + a_1a_2}\eta(s)\\ &= \frac{\left(\frac{1}{\mathcal{M}_1+\mathcal{M}_2}s + \frac{1}{(\mathcal{M}_1+\mathcal{M}_2)T_{g1}}\right)\eta(s)}{s^2 + \left(\frac{1}{T_{g1}} + \frac{D_1+D_2}{\mathcal{M}_1+\mathcal{M}_2}\right)s + \frac{D_1+D_2+k_{g1}R_1^{-1}}{(\mathcal{M}_1+\mathcal{M}_2)T_{g1}}}\end{aligned} \tag{19}$$

where a_1 and a_2 are the poles, c_1 and c_2 are the residues, and $\eta(s) = b_1^{\text{lf}}(s) + b_2^{\text{lf}}(s)$. From (19) we see that $\mathcal{G}_M = \mathcal{M}_1 + \mathcal{M}_2$ can be derived through the $c_1 + c_2$ term by performing an *experiment*.[8] Let us assume to vary $\mathcal{M}_1$ of a known constant value $\Delta\mathcal{M}$ (varying $\mathcal{M}_2$ is totally equivalent). This variation does not alter the power flow solution of the system but how the rotor speed of the G_1 generator reacts to power imbalances. Before the experiment, we have $c_1 + c_2 = (\mathcal{M}_1 + \mathcal{M}_2)^{-1}$ (see the coefficient of the s term at the numerator of the second and third expressions of (19)) and after the experiment $\hat{c}_1 + \hat{c}_2 = (\mathcal{M}_1 + \mathcal{M}_2 + \Delta\mathcal{M})^{-1}$, from which we derive

$$\mathcal{G}_M = \frac{\hat{c}_1 + \hat{c}_2}{c_1 + c_2 - \hat{c}_1 - \hat{c}_2}\Delta\mathcal{M}\ . \tag{20}$$

At first we perform a proper frequency scan of the system (limited to a low frequency range, where generators are synchronized) by acting on either $b_1(t)$ or $b_2(t)$ (or both) to numerically derive (18). Then, we use the VF technique [30–32] to fit (19) and determine the pairs of c_1, c_2 and $\hat{c}_1$ and $\hat{c}_2$ coefficients (i.e., before and after the experiment) and, thus, $\mathcal{G}_M$.

This approach presents several drawbacks. First and foremost, in practice it is typically not possible to act on the inertia constant of the synchronous machines. Secondly, a complete frequency scan is also unfeasible. Lastly, the rotor speed of the synchronous machines is unlikely to be available. In the following, we show how to overcome these issues.

[8] Even this very simple power system is governed by a set of nonlinear ODEs (see (15)). The small-signal equivalent model of (15) can be written in closed form, but Eq. (18) can be derived only by approximating the coefficients of Eq. (17), as we described in Section 3.1. This means that, even if we were able to control $b_1(s)$ and $b_2(s)$, the $\eta(s)$ input in (19) is not directly controlled since we should be able to derive how $b_1(s)$ and $b_2(s)$ split to $b_1^{\text{lf}}(s)$ and $b_2^{\text{lf}}(s)$. As a consequence, the $\eta(s)$ cannot be separated out in the overall coefficient of s in the last equation of (19), and the *experiment* is needed.

4. Global inertia estimation: a method

The *experiment* described in Section 3.2 can be implemented by resorting to a grid-forming (GF) converter-interfaced generator (CIG) (see ① in Fig. 3). This device may already be present in the power system or can alternatively be inserted with the specific purpose of allowing the estimation of the power system global inertia. As shown in Section 5, the state equations governing the dynamics of this device are similar to those reported in (1). Hence its equivalent rotor speed ω_{gf} becomes one of the entries of the $\boldsymbol{\omega}$ vector and its equivalent inertia constant one of the diagonal elements of the $\boldsymbol{\mathcal{M}}$ matrix. Proper low-frequency small-signal tones injected through the GF CIG itself can contribute to the $\mathbb{1}_{1,N}\boldsymbol{b}^{\text{lf}}(s)$ term in Eq. (14). By observing the frequency response of the equivalent rotor speed of the GF CIG, once those tones are injected, we can obtain a proper set of samples of (14). We recall that (14) provides the expression in the Laplace domain shared (at low frequency) by all the components of $\boldsymbol{\omega}$ and hence of ω_{gf}. By varying the GF CIG equivalent inertia constant and fitting the samples of (14) before and after this variation, it is possible to derive the *global inertia* of the entire power system.

We underline that the reader must not be confused at this point: by injecting small-signal power perturbations through the CIG and measuring its virtual rotor speed, *we do not estimate the* CIG *virtual contribution to the overall system inertia*, as it is done in several papers in the literature. On the contrary, we estimate the *global inertia* of the entire power system (CIG included). In other words, the CIG can be viewed as a probing-signal source, whose virtual inertia is known and can be modified during the experiment needed to obtain $\mathcal{G}_M$.

The method we developed gives a continuous estimate of the global inertia and is summarized in the flowchart of Fig. 3. Since we use the VF algorithm [30–32] to estimate the residues and the poles of (14), we need frequency samples of both its modulus and phase. This forbids resorting to the power spectral density of ω_{gf} when its fluctuation is solely given by the noisy generated/absorbed powers. We thus opted to modulate the power injected by the CIG by a discrete set of $\mathcal{N}_\mathcal{T}$ deterministic and coherent small-signal sinusoidal tones $s_w(t)$ ($w = 1, \dots, \mathcal{N}_\mathcal{T}$). The choices of $\mathcal{N}_\mathcal{T}$ and of the f_w frequency of each tone depend on the bandwidth that has to be explored to fit (14) (see ② in Fig. 3). It is worth mentioning that $\mathcal{N}_\mathcal{T}$ must be fixed in excess with respect to the residues and poles number of (14). The $s_w(t)$ tones are very slowly varying and of modest magnitude [45–47], therefore they do not impact the stability of the power system. Such tones were designed by exploiting the Crest Factor Minimization approach presented in [45–47].

The equivalent inertia constant of the CIG varies as a square waveform of amplitude $\Delta\mathcal{M}$, period $T_{\Delta\mathcal{M}}$, and duty cycle 50%. The power system is stimulated by injecting the $s_w(t)$ waveforms and the time samples of ω_{gf} are collected (see ③ in Fig. 3). We computed the γ_{w_c} and γ_{w_s} direct and quadrature components of the Fourier integrals of ω_{gf} at each f_q frequency as (see ④ in Fig. 3)

$$\begin{aligned}\gamma_{w_c} &= \frac{f_w}{\mu}\int_{t_0}^{t_0+\frac{\mu}{f_w}} \omega_{\text{gf}}(t)\cos(2\pi f_w t)dt\\ \gamma_{w_s} &= \frac{f_w}{\mu}\int_{t_0}^{t_0+\frac{\mu}{f_w}} \omega_{\text{gf}}(t)\sin(2\pi f_w t)dt\ .\end{aligned} \tag{21}$$

The γ_{w_c} and γ_{w_s} terms constitute the frequency samples that feed the VF algorithm (see ⑤ in Fig. 3). Note that if it is necessary to reduce the effects of noise to increase the signal-to-noise ratio, the integrals in (21) can be computed over a time interval μ/f_w which is a multiple of the period of the corresponding tone $s_w(t)$. The t_0 time instant in (21) coincides with the rising and falling edges of the square waveform used to periodically change the virtual inertia of the CIG. Assuming $s_1(t)$ as the tone with the lowest frequency, f_1 suggests how to choose $T_{\Delta\mathcal{M}}$, i.e., $T_{\Delta\mathcal{M}}/2 > \mu/f_1$.

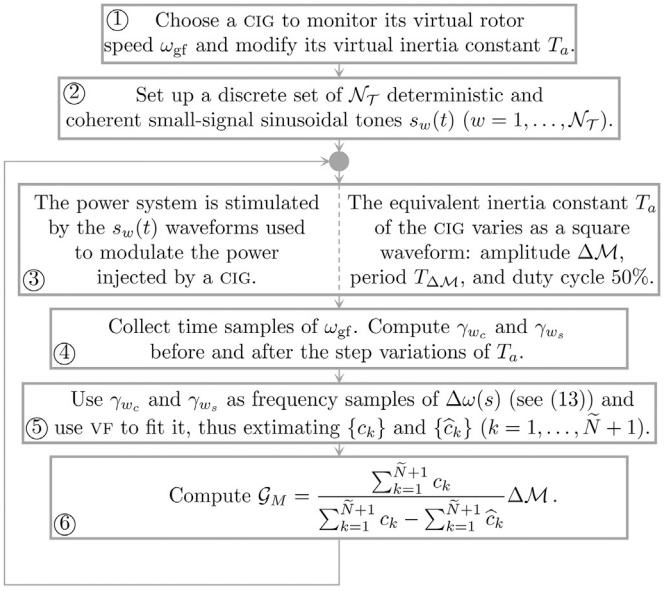

Fig. 3. The flow chart of the proposed method. Steps from ③ to ⑥ are periodically repeated.

As shown in the next section, the proposed estimation method can be applied to bigger power systems than that shown in Fig. 1 by resorting to (14). Indeed, also (14) can be recast through a partial fraction decomposition analogous to (19). Thus, even in more complex cases, the process to estimate the global inertia still relies on (20) (see ⑥ in Fig. 3) and vector fitting.

5. Numerical examples

5.1. Virtual synchronous generator

A grid-forming (GF) converter-interfaced generator (CIG) implements a control scheme that simulates the mechanical dynamical behavior of a synchronous machine (swing equation) by means of a power converter. Among others, this implementation can provide inertia, damping, and primary frequency control — features that are particularly useful in grids with a significant penetration of renewable energy sources and therefore reduced inertia.

The proposed approach to estimate the $\mathcal{G}_M$ global inertia exploits the GF CIG model described in [29]. By adopting an average inverter model equipped with an LC filter and vector current control, it provides virtual inertia by implementing the swing equation with frequency droop control and replicates the stator impedance of the synchronous generator. Importantly, the vast majority of CIGs that provide synthetic inertia reproduce the mechanical behavior of a synchronous machine (i.e., the swing equation), but also add the dynamics of the electronic converters, given by its controls and filters: so doing, they fail to replicate the full electro-mechanical behavior of synchronous machines due to windings, including dampers. The CIG model in [29] belongs to this category and therefore implements only the swing equation, leading to a different spectral footprint at high frequencies with respect to a real synchronous generator. In our simulations, we implemented and used the full model detailed in [29]. For the sake of brevity, hereafter we report only its implementation of the swing equation

$$\begin{aligned} \dot{\delta}_{gf} &= \Omega\left(\omega_{gf} - \omega_0\right) \\ 2T_a\dot{\omega}_{gf} &= \left(1+\eta_{gf}\right)P_g - P_e - K_d\left(\omega_{pll} - \omega_{gf}\right) - K_w\left(\omega_{gf} - \omega_0\right), \\ P_e &= (V_d I_d + V_q I_q) S_{ref}^{-1} \end{aligned} \quad (22)$$

where V_d, I_d, V_q, and I_q are the voltages and currents of the generator in the dq-frame that lead to the P_e electrical active power (pu), S_{ref} is the power rating of the CIG, T_a is the (virtual) inertia constant, P_g is the generated power setpoint at system frequency ω_0 (pu), K_w is the load damping, δ_{gf} is the angle deviation of the virtual rotor, ω_{gf} is the virtual rotor angular speed (pu), ω_{pll} is the electrical angular frequency of the voltage at the connection bus (pu), K_d regulates the virtual rotor speed according to the electrical angular frequency of the bus to which the CIG is connected, thus emulating frequency slip (in our case, $K_d = 0$). η_{gf} is the small signal used to perturb the power system, which modulates the active power setpoint of the CIG.

5.2. Load models

The lth load model (for $l = 1, \ldots, L$) is

$$\mathrm{L}_l = \left(1 + \eta_l(t)\right) P_{\mathrm{L}0_l} \left(\frac{|V_l|}{V_{0_l}}\right)^{\gamma}, \quad (23)$$

where $P_{\mathrm{L}0_l}$ is the nominal active power of the load, V_{0_l} is the load voltage rating, V_l is the bus voltage at which the load is connected, and γ governs the dependence of the load on bus voltage (hereafter assumed to be null). By applying the $\eta_l(t)$ small signal, we can perturb the load power.

In the time domain simulations of stochastic load fluctuations, we assume that $\eta_l(t)$ is an Ornstein-Uhlenbeck (OU) process [40]. The OU processes (one for each load) are defined through the set of stochastic differential equations (SDEs)

$$d\boldsymbol{\eta} = -\boldsymbol{\Upsilon}\boldsymbol{\eta}\, dt + \boldsymbol{\Sigma}\, d\boldsymbol{W}_t, \quad (24)$$

where the drift $\boldsymbol{\Upsilon} \in \mathbb{R}^{L\times L}$ and diffusion $\boldsymbol{\Sigma} \in \mathbb{R}^{L\times L}$ are diagonal matrices with positive entries, $\boldsymbol{W}_t \in \mathbb{R}^L$ is a vector of Wiener processes, and the differentials rather than time derivatives are utilized to account for the idiosyncrasies of SDEs. The L OU processes are characterized by a mean-reversion property and exhibit bounded standard deviation that can be written as $\sigma_l^2/(2\upsilon_l)$, for $l = 1, \ldots, L$, where σ_l and υ_l are the diagonal elements of $\boldsymbol{\Sigma}$ and $\boldsymbol{\Upsilon}$, respectively [48]. Moreover, these processes show a spectrum that is an accurate model of the stochastic variability of power loads [40,42,49,50].

To carry out the simulations discussed below, the numerical integration of the multi-dimensional OU process in (24) was based on the numerical scheme proposed by Gillespie in [51]. Furthermore, the second-order trapezoidal implicit weak scheme for stochastic differential equations with colored noise [52], available in the simulator PAN [53–55], was adopted.

5.3. The IEEE 39-BUS test system

We used as first benchmark a modified version the IEEE 39-BUS system [56]. The grid contains 10 generators and 46 lines and is a simplified model of the New England power system. Its schematic is reported in Fig. 4. The G_1 generator models the aggregate behavior of a large number of generators. This is reflected in its inertia value, which is one order of magnitude larger than that of the other generators in the grid (see Table 2). The IEEE 39-BUS system version we started from is that in the distribution of POWERFACTORY by DIGSILENT.

We also inserted three CIGs at BUS8, BUS14 and BUS27 (highlighted in red in Fig. 4), which respectively model an aggregated wind power plant, and two battery storage systems. Each CIG is characterized by a 50 s inertia constant, with $P_g = 1$ pu and $S_{ref} = 100$ MVA (see (22)). In particular, the CIG used for the experiment is the one connected at BUS14. It is worth pointing out that there is not a preferred bus to which one should connect the CIG used for this purpose. In any case, the proposed estimation algorithm takes into account every component affecting the global inertia (including the synthetic inertia contributed by CIGs). In this case study, $\mathcal{G}_M = 186.4$ GVAs, 30 GVAs of which are contributed by the three GF CIGs as a whole.

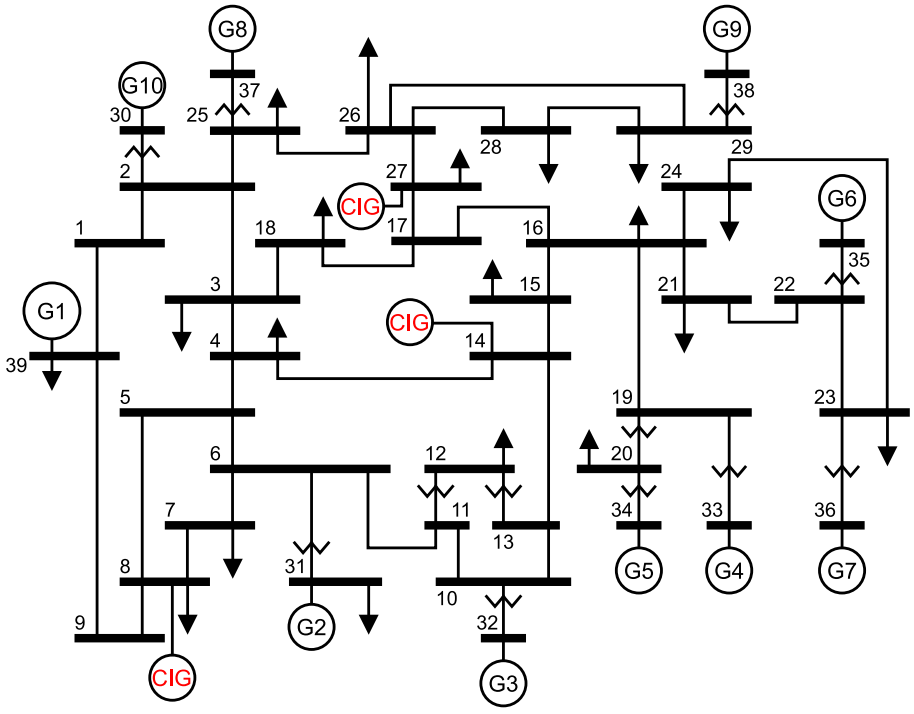

Fig. 4. Schematic of the modified IEEE 39-BUS system. The CIGs are highlighted in red.

Table 2
Synchronous generators H and S_B ($S_{\text{base}} = 100\,\text{MVA}$).

Gen.	H [s]	S_B [pu]	Gen.	H [s]	S_B [pu]
G_1	5.00	100	G_6	4.35	8
G_2	4.33	7	G_7	3.77	7
G_3	4.47	8	G_8	3.47	7
G_4	3.57	8	G_9	3.45	10
G_5	4.33	6	G_{10}	4.20	10

Firstly, we performed an (ideal) *frequency scan*[9] assuming $\eta_{\text{gf}}(t)$ as a small-signal sinusoidal source and by turning off the stochastic variations of the loads. So doing, we computed all the transfer functions between $\eta_{\text{gf}}(t)$ and the rotor speed of each synchronous machine and CIG. Fig. 5 (upper panel) reports these transfer functions. We can notice that they almost perfectly overlap at frequencies below 0.1 Hz while they sensibly differ for higher frequency values. This result carries similar information as that in Fig. 2. Note that these transfer functions show how rotor speeds deviate from ω_0 under the assumption of small-signal behavior (linear behavior in the neighborhood of the equilibrium point, i.e., power-flow). These spectra show that if we think of a step perturbation, during the first time interval after its application, say

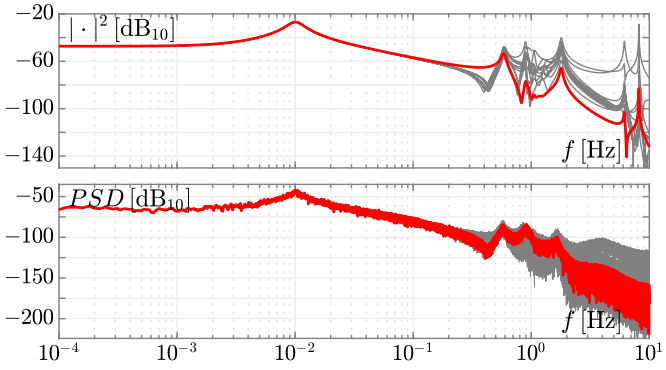

Fig. 5. Upper panel: the magnitude squared of the transfer functions between $\eta_{\text{gf}}(t)$ and the rotor speed of each synchronous machine and CIG of the (modified) IEEE 39-BUS system. Lower panel: power spectral densities of the rotor speed of each synchronous machine and CIG of the (modified) IEEE 39-BUS system when the stochastic noise in the loads is turned on. In both panels the red curve refers to the CIG connected at BUS14.

0.1 s → 10 Hz, the synchronous generators lose synchrony and counteract power imbalance in a non-coordinated way. This behavior persists up to 2 s → 0.5 Hz, at which point the synchronous generators and CIGs go toward re-synchronization (low frequency behavior). By observing the low frequency overlapping of all the curves in Fig. 5, the global inertia can be determined through (14) by fitting *only* the curve related to the CIG connected at BUS14 in the $[6, 33]$ mHz frequency interval, since all rotor speeds are described by the same behavior in this frequency interval (principal frequency system dynamics), as predicted by our analysis. The frequency behavior in this band is exclusively due to the mechanical characteristics of the power system contributed by synchronous generators and prime movers (swing equation) and by CIGs that implement virtual inertia.

[9] In the conventional frequency scan, the power system is linearized at its power flow solution and, by resorting to the Jacobian matrices of the differential algebraic equations (DAEs) governing the dynamics of the power system model, the frequency response of the (linearized) system to a pure sinusoidal-tone injection is computed. This implements the well known AC small-signal analysis technique. If one considers the simpler case in which the power system is governed by a set of ODEs, starting from (1) and its linearization reported in (2), the injection through the CIG of $\eta_{\text{gf}}(t)$ yields the formulation reported in (9). By transforming the latter in the Laplace domain, similarly to what was explicitly done for $\boldsymbol{\Delta\omega}(t) = \Delta\omega(t)\mathbb{1}_{N,1}$ (see (10)), the transfer functions between any element of $\boldsymbol{b}$ and any element of $\boldsymbol{\Delta\omega}$ can be derived.

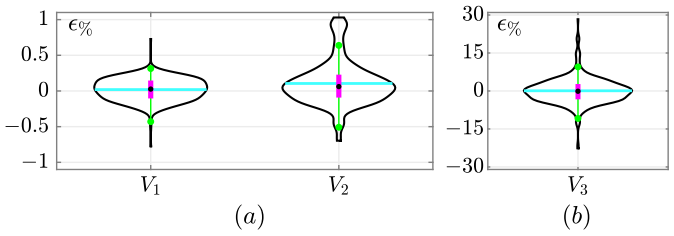

Fig. 6. Inertia estimation results obtained by applying the proposed method to the IEEE 39-BUS test system. Panel (a). The V_1 violin plot ($\mu = 0.019$, $\mu_{\text{dn}} = 0.026$, and IQR = 0.232) refers to the results obtained by exploiting an ideal frequency scan assuming $\eta_{\text{gf}}(t)$ as a small-signal sinusoidal source. The V_2 violin plot ($\mu = 0.105$, $\mu_{\text{dn}} = 0.062$, and IQR = 0.302) refers to the results obtained by injecting a set of $\mathcal{N}_{\mathcal{T}} = 10$ deterministic and coherent small signal sinusoidal tones through the CIG connected at BUS14. Both V_1 and V_2 were obtained by assuming all the loads as noiseless.
Panel (b). Contrary to V_2, the V_3 violin plot ($\mu = 0.074$, $\mu_{\text{dn}} = -0.104$, and IQR = 5.48) was derived by turning on the stochastic noise in the loads.

We exploited this frequency scan to estimate the global inertia of the IEEE 39-BUS system. We performed 500 independent frequency scans and for each of those the inertia constant of each generator was uniformly randomly varied by ±30% with respect to its nominal value. This was done to test the method on a large set of inertia configurations.[10] At each run, we used the VF method to fit the frequency behavior of the CIG virtual rotor angular frequency before and after the experiment and estimated the $\mathcal{G}_M$ global inertia. The left violin plot in Fig. 6(a) summarizes the performance of the proposed approach, in terms of the $\epsilon_{\%} = 100\frac{\mathcal{G}_M - \mathcal{G}_M^{\text{act}}}{\mathcal{G}_M^{\text{act}}}$ percent relative error, in estimating $\mathcal{G}_M$ for each one of the 500 random configurations w.r.t. its actual value $\mathcal{G}_M^{\text{act}}$. In Fig. 6(a), as in all the violin plots reported in the sequel, the horizontal cyan segments and the black solid circle markers correspond to the mean μ and the median μ_{dn} of the results, respectively. The magenta bars represent the IQR, viz. the spread difference between the 75th and 25th percentiles of the data. The green solid circle markers represent the upper adjacent value (i.e., the largest observation that is less than or equal to the third quartile plus 1.5 × IQR) and the lower adjacent value (i.e., the smallest observation that is greater than or equal to the first quartile minus 1.5 × IQR).

As mentioned before, given that this ideal frequency scan is not practical, we turned on the injection of the discrete set of $\mathcal{N}_{\mathcal{T}} = 10$ deterministic and coherent small-signal sinusoidal tones by the CIG connected at BUS14. We performed 500 time domain analyses again by randomly varying the inertia configuration and performed the experiment (as well as all the steps detailed in Section 4 and Fig. 3) to compute the global inertia. As previously stated, by considering the $s_1(t)$ tone with the lowest frequency f_1, the time window of the estimation method should be such that $T_{\Delta\mathcal{M}}/2 > \mu/f_1$ (see Fig. 7). Since the frequency[11] of the slowest injected-tone was 6 mHz (i.e., the lower bound of the frequency range over which we fit the virtual rotor speed spectrum of the CIG connected at BUS14), a time window $T_{\Delta\mathcal{M}}/2$ of at least $\mu/f_1 \approx 340$ s is needed to compute the Fourier integrals in (21) with $\mu = 2$. This time interval is necessary for both $\Delta\mathcal{M} = 0$ and $\Delta\mathcal{M} > 0$ (see Fig. 3). To perform a more reliable estimation, we extended this interval of $\Delta T_{\text{tr}} = 110$ s to account for possible transients after the $\Delta\mathcal{M}$ step (thus leading to $T_{\Delta\mathcal{M}}/2 = 450\,\text{s} \approx 7.5$ min). The estimation procedure (i.e., the application of the VF and (20)) requires $\Delta T_{\mathcal{G}_M} < 10$ s. Overall, each simulation was carried out for an up rounded time window of $T_{\Delta\mathcal{M}} = 2\left(\mu/f_1 + T_{\text{tr}}\right) \approx 15$ min. It is worth noticing that, after the first two estimations, which represent some sort of "start-up" phase, one could use the procedure in Fig. 3 to estimate global inertia by exploiting also the transition from $\Delta\mathcal{M} > 0$ to $\Delta\mathcal{M} = 0$. So doing, the algorithm provides an estimate every $T_{\Delta\mathcal{M}}/2$ of the power system evolution. This is sketched in Fig. 7 where the $\Delta T_{\mathcal{G}_M}$ narrow shaded windows refer to the estimation phase performed after a step in the inertia of the GF CIG used to probe the grid, while the ΔT_{tr} wide shaded windows, partially overlapping to the former, refer to the dead-time used to account for transients. Each time the estimation phase begins, we only collect the data associated with non-shaded windows of the previous $T_{\Delta\mathcal{M}}$ period that are necessary to compute the Fourier integrals and, thus, estimate inertia. Note that probing signals must be continuously injected during the time interval in which one is interested in estimating $\mathcal{G}_M$.

The information of the $\epsilon_{\%}$ percent relative error in estimating the global inertia are shown by the right violin plot in Fig. 6(a). We can notice that the overall performance is worsened even if it remains very good since the relative error in determining the global inertia is in any case lower than 1.0%.

Finally we turned on the stochastic noise in the loads. In the lower panel of Fig. 5, we report the frequency behavior of the rotor speed of all the synchronous machines and CIGs when all the loads of the grid are perturbed as described in Section 5.2.

We used $L = 19$ independent η_l small-signal stochastic noise sources, one for each power load. We choose $\upsilon_l = 0.5$ and set σ_l (see (24) and related text) in such a way that the standard deviation of $\eta_l(t)$ is 0.5% of P_{L0_l} (nominal load active power) in (23). The zero mean implies that on average the stochastic loads power fluctuations do not perturb the operating point of the system. By observing the spectral densities in Fig. 5 (lower panel), we notice a different behavior of the rotor speed deviations at frequency above 100 mHz but once more spectra almost perfectly overlap at lower frequencies. This means that the effect of the stochastic noise sources will be superimposed to that of the $\mathcal{N}_{\text{T}}$ tones injected by the CIG.

We ran 500 time-domain large-signal simulations with the nominal inertia configuration and with a magnitude of the injected tones that cause a peak power variation less than 2.5% of the nominal power of the IEEE 39-BUS system. The violin plot giving information about the relative error in the global inertia estimation is shown in Fig. 6(b). We see that the relative error is further increased with respect to the previous cases. This is due to the decreased signal-to-noise-ratio (SNR) that makes more difficult the fitting of Eq. (14) with the VF method. Nonetheless, the mean and median estimation error are respectively $\mu = 0.074$ and $\mu_{\text{dn}} = -0.104$, which proves that the method is quite robust with respect to noise.

5.4. *The* IEEE 118-BUS *test system*

As a second benchmark, we used the IEEE 118-BUS system. It represents an approximation of the American Electric Power system (in the U.S. Midwest) as of December 1962. It contains 19 generators, 35 synchronous condensers, 177 lines, 9 transformers, and 91 loads. The original model is available in the distribution of MATPOWER [57], but it does not contain any dynamic model. There are several versions enhanced with dynamic models; guidelines can be found in [58].

The only GF CIG connected to the grid is the one used to generate the perturbing power tones and perform the experiment. It is connected at BUS38 and is characterized by a 25 s inertia constant, with $P_g = 1$ pu and $S_{\text{ref}} = 300$ MVA. As already said for the IEEE 39-BUS, there is not a preferred bus to which the CIG used for the experiment should be connected. Some more comments on this aspect, as well as others related to the implementation of the proposed method, are given in Section 6.

The result of the (ideal) frequency scan obtained by assuming $\eta_{\text{gf}}(t)$ as a small-signal sinusoidal source is shown in Fig. 8. We see that as for the IEEE 39-BUS system all the angular frequencies of synchronous

[10] Some of these configurations can lead to (almost) identical global inertia values but with different partitions among each synchronous generator and CIG.

[11] The fundamental frequencies of the 10 deterministic and coherent small-signal sinusoidal tones injected both in the (modified) IEEE 39-BUS and in the IEEE 118-BUS system are $\{6, 9, 12, 15, 18, 21, 24, 27, 30, 33\}$ mHz.

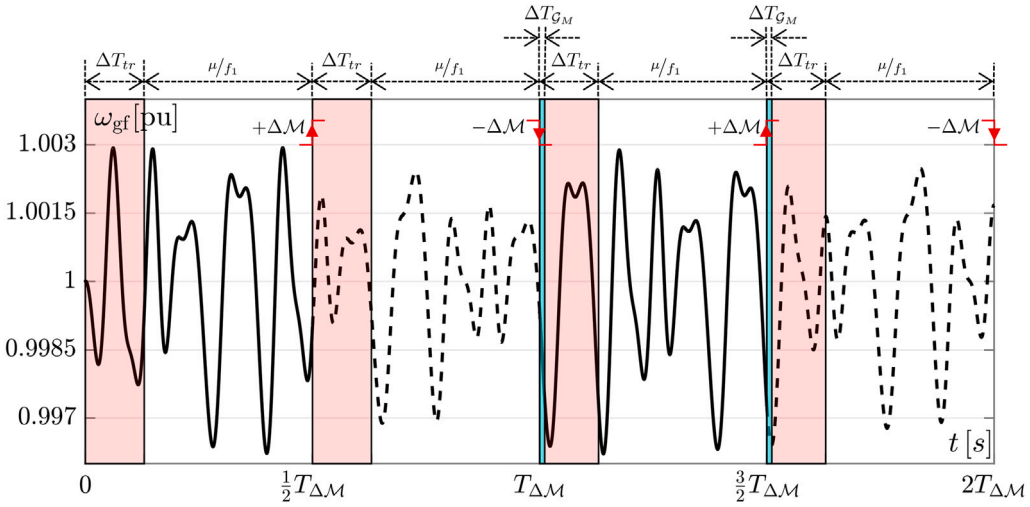

Fig. 7. Two full periods $T_{\Delta\mathcal{M}}$ of the GF CIG inertia constant modulation are sketched assuming the estimation procedure starting at $t = 0$. The ΔT_{tr} wide shaded windows refer to the dead-time used to account for transients. The estimation procedure is carried out during the $\Delta T_{\mathcal{G}_M}$ narrow shaded windows that overlap the ΔT_{tr} ones. The whole estimation procedure is at steady state after $T_{\Delta\mathcal{M}}$: after that, new estimates are provided every $\frac{\Delta T_{\Delta\mathcal{M}}}{2}$ seconds.

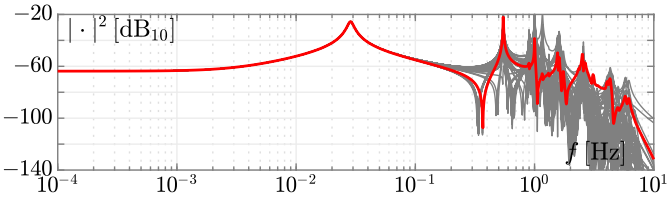

Fig. 8. The magnitude squared of the transfer functions between $\eta_{\mathrm{gf}}(t)$ injected through the GF CIG connected at BUS38 and the rotor speed of each synchronous machine and CIG of the (modified) IEEE 118-BUS system. The red curve refers to the (virtual) rotor speed of the CIG connected at BUS38.

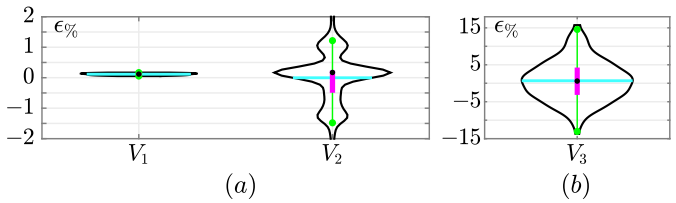

Fig. 9. Inertia estimation results obtained by applying the proposed method to the IEEE 118-BUS test system. The simulation setup for the V_k violin plot ($k \in \{1, 2, 3\}$) is the same one of the kth violin plot in Fig. 6. Thus, for each violin plot, only the values of mean μ, median μ_{dn}, and IQR are briefly reported. Panel (a). V_1 violin plot: $\mu = 0.115$, $\mu_{\mathrm{dn}} = 0.117$, and IQR = 0.055. V_2 violin plot: $\mu = -0.002$, $\mu_{\mathrm{dn}} = 0.170$, and IQR = 0.680. Panel (b). V_3 violin plot: $\mu = 0.675$, $\mu_{\mathrm{dn}} = 0.592$, and IQR = 7.01.

machine rotors and CIG overlap almost perfectly at low frequency (<100 mHz).

In this case study, $\mathcal{G}_M = 116.4$ GVAs (7.5 GVAs of which is contributed by the GF CIG. We thus repeated the same simulations of the IEEE39 system: for each of the 500 runs we carried out, we estimated the global inertia by a frequency scan, then also in the time domain with noiseless loads and, lastly, with noisy loads. As before, in the first and second case, the inertia of each generator was uniformly randomly varied of ±30% with respect to its nominal value, while in the third case the nominal inertia configuration was considered.

The results are summarized by the violin plots in Fig. 9 and have the same meaning of those in Fig. 6. We see that very good estimation results of global inertia are obtained also for the IEEE 118-BUS system.

6. Discussion and conclusion

We highlight hereafter key differences between some inertia estimation methods proposed in the literature and our proposed method, which should better clarify the points of strength and novel features of the latter.

Among others, the works in [7,59] rely on active power and frequency measurements coming from the PMUs installed at each generation bus to estimate the inertia of an area. They require knowing in advance where and if synchronous generators (and GF CIGs providing virtual inertia) are connected. This has limited utility in practice, since the TSO/DSO usually knows if a synchronous generator is connected — and, if so, its inertia, too. At best, these methods can be useful if there are (small) generators of unknown characteristics (e.g., whose inertia has to be identified for the first time) or, in case of GF CIGs, if the ancillary services related to frequency support need to be rewarded based on the effective value of virtual inertia provided at a given time.

A few methods [59,60] estimate the total inertia of an area but often need measurements of the instantaneous active power flowing to/from the area. In particular, area power exchange is usually required to flow through a single connection (line) to ensure a reliable estimation. Moreover, these solutions need to estimate the rotor speed of each synchronous generator and GF CIG, which implies that generation unit location must still be known in advance.

In [61], convolutional neural networks (CNNs) are used to estimate the power system momentum. However, as with most machine-learning-based methods, this requires a large dataset used for training the method and ensure adequate estimation capabilities (i.e., a low prediction error), which in general may not be easily available. Moreover, if CNNs have to estimate the inertia of a power system which includes new elements that were not included in the dataset and, most importantly, whose frequency response following power mismatches has a different footprint from the other generation units, estimation results may be inaccurate.

On the contrary, our method needs no information as to the point of connection of synchronous generators and GF CIGs. In other words, the proposed method is agnostic with respect to the system, and can

estimate the global momentum of the grid, which is given by summing up all the contribution in terms of inertia given by synchronous generators/motors, synchronous condensers, and grid-forming or grid-following CIGs providing virtual inertia of any capacity. The proposed solution collects only the virtual rotor speed measurements of one GF CIG. This GF CIG has to be under control of the user, since it has to inject probing tones in the electric grid and alter the amount of virtual inertia it provides. In view of a practical implementation, we do think that these requirements are largely feasible. In case one tried to extend the estimation procedure to work with the electrical frequencies measured at the power system buses (e.g., by exploiting PMUs), the source of the input data could be an issue that one should properly take into account. In any case, since the frequency band of interest is at low frequency, we do not expect measurement equipment to be a bottleneck of the proposed approach. For what concerns probing of (virtual) rotor speed of generators, it is not an issue since as already underlined we get the low frequency behavior which is shared by the entire power system.

Throughout this work, we specified that there is not a preferred bus to which one should connect the GF CIG used for signal probing and inertia modulation. To validate this statement, we performed several simulations of the systems under study (and also others) to investigate the impact of the probing GF CIG position in the grid on inertia estimation. These preliminary analyses neither let us derive any specific rule to choose the position of this device nor revealed a particular criticality in applying the proposed approach. From a theoretical standpoint, as soon as the power system model behaves as a synchronized power-controlled oscillator, the location of the probing GF CIG is not an issue for what concerns the principal frequency dynamics, viz. in term of synchronization at low frequency, since the low frequency behavior is shared by all the synchronous generators/motors and GF CIGs.

However, it is the concept itself of total amount of inertia or better of global power system momentum, if used as a "stability index", that has to be put under the spotlight. As it can be seen from Figs. 5 and 8, the spectra split at high frequency and almost perfectly overlap at low frequency. In the time domain this means that right after a disturbance (e.g., a consistent local power imbalance at a bus) occurs, frequency support is first *locally* given by generators/condensers and GF CIGs that are electrically near the point where the disturbance occurs. Since synchronization is not achieved immediately, synchronous machines and CIGs may react differently to the disturbance. Thus, their response can be uncoordinated with one another at first. Indeed, only with time the frequency support slowly propagates by spreading to the entire power system, whose generation units eventually re-synchronize (low frequency portion of the spectrum in Figs. 5 and 8). As a result, the fast "local" support following a power imbalance can be inadequate to avoid intervention of under-frequency relays, even though the global momentum of the grid is more than satisfactory. This suggests that in a large power grid with several areas that are "electrically" far, an adequate level of "local" inertia has to be ensured in each area to obtain a corresponding adequate frequency support [62]. We believe that this concept is novel and its determination is still an open issue, but out of the scope of this paper.

In the simulation results we showed that the proposed method is robust to noise. In general, the tones injected by the GF CIG must have an adequate amplitude, otherwise the intrinsic noise due to random power fluctuations by loads and generations may lead to a too low signal-to-noise ratio. As a matter of fact, the effects of the $\Delta\mathcal{M}$ step variation of the virtual inertia of the GF CIGs must be accurately detected by revealing its effects on the injected tones. These tones are extracted from the noise floor by exploiting the Fourier integrals on a suitable time window. Since the noise has a zero mean value, undesired effects that noise may yield on inertia estimates can be mitigated by acting on the time window $T_{\Delta\mathcal{M}}$: the longer it is, the higher the signal-to-noise ratio and the more robust the inertia estimates. However, this negatively affects the update rate of global momentum estimation. Moreover, longer time windows can potentially suffer of fluctuations of (virtual) inertia over an half of a time window and worsen the estimation. As suggested above, another solution to reduce the effects of noise consists in using probing signals of higher amplitude. To this aim, one could rely on a single large GF CIG or the synchronized injection of probing tones through multiple GF CIGs of smaller capacity. The latter solution may be more reliable and allows exploiting existing GF CIG scattered in the power system. Future research work is going to be devoted to these aspects.

CRediT authorship contribution statement

Angelo Maurizio Brambilla: Writing – review & editing, Writing – original draft, Software, Methodology, Investigation, Formal analysis, Conceptualization. **Davide del Giudice:** Writing – review & editing, Writing – original draft, Software, Methodology, Investigation, Formal analysis, Conceptualization. **Daniele Linaro:** Writing – review & editing, Writing – original draft, Software, Methodology, Investigation, Formal analysis, Conceptualization. **Federico Bizzarri:** Writing – review & editing, Writing – original draft, Software, Methodology, Investigation, Formal analysis, Conceptualization.

Declaration of competing interest

All authors have participated in

(1) conception and design, or analysis and interpretation of the data;

(2) drafting the article or revising it critically for important intellectual content;

(3) approval of the final version.

This manuscript has not been submitted to, nor is under review at, another journal or other publishing venue.

The authors have no affiliation with any organization with a direct or indirect financial interest in the subject matter discussed in the manuscript.

Data availability

Data will be made available on request.

Appendix A

To derive the $\boldsymbol{v}_1$ left-eigenvector reported in (5) we write

$$\boldsymbol{A}^{\mathrm{T}} = \begin{bmatrix} \mathbb{O}_N & -\boldsymbol{\Pi}\boldsymbol{\mathcal{M}}^{-1} & \mathbb{O}_N \\ \Omega\mathbb{1}_N & -\boldsymbol{\mathcal{M}}^{-1}\boldsymbol{D} & -\boldsymbol{T}_g^{-1}\boldsymbol{k}_g\boldsymbol{R}^{-1} \\ \mathbb{O}_N & \boldsymbol{\mathcal{M}}^{-1} & -\boldsymbol{T}_g^{-1} \end{bmatrix} \tag{A.1}$$

and we have to solve $\boldsymbol{A}^{\mathrm{T}}\boldsymbol{v}_1 = \mathbb{O}_{3N,1}$. By choosing $\boldsymbol{v}_1 = (\boldsymbol{v}_\delta^{\mathrm{T}}, \boldsymbol{v}_\omega^{\mathrm{T}}, \boldsymbol{v}_{P_m}^{\mathrm{T}})^{\mathrm{T}}$, this implies

$$\begin{cases} -\boldsymbol{\Pi}\boldsymbol{\mathcal{M}}^{-1}\boldsymbol{v}_\omega = \mathbb{O}_{N,1} \\ \Omega\boldsymbol{v}_\delta - \boldsymbol{\mathcal{M}}^{-1}\boldsymbol{D}\boldsymbol{v}_\omega - \boldsymbol{T}_g^{-1}\boldsymbol{k}_g\boldsymbol{R}^{-1}\boldsymbol{v}_{P_m} = \mathbb{O}_{N,1} \\ \boldsymbol{\mathcal{M}}^{-1}\boldsymbol{v}_\omega - \boldsymbol{T}_g^{-1}\boldsymbol{v}_{P_m} = \mathbb{O}_{N,1} \end{cases} .$$

From the first equation above, being $\ker(\boldsymbol{\Pi}) = \mathbb{1}_{N,1}$, we find $\boldsymbol{v}_\omega = \boldsymbol{\mathcal{M}}\mathbb{1}_{N,1}$. Hence, from the third equation, $\boldsymbol{v}_{P_m} = \boldsymbol{T}_g\mathbb{1}_{N,1}$, and, from the second one, $\boldsymbol{v}_\delta = \Omega^{-1}(\boldsymbol{D} + \boldsymbol{k}_g\boldsymbol{R}^{-1})\mathbb{1}_{N,1}$. Since $\boldsymbol{u}_1 = [\mathbb{1}_{1,N}, \mathbb{O}_{1,2N}]^{\mathrm{T}}$, then

$$\boldsymbol{v}_1^{\mathrm{T}}\boldsymbol{u}_1 = \Omega^{-1}\mathbb{1}_{1,N}\left(\boldsymbol{D} + \boldsymbol{k}_g\boldsymbol{R}^{-1}\right)\mathbb{1}_{N,1} ,$$

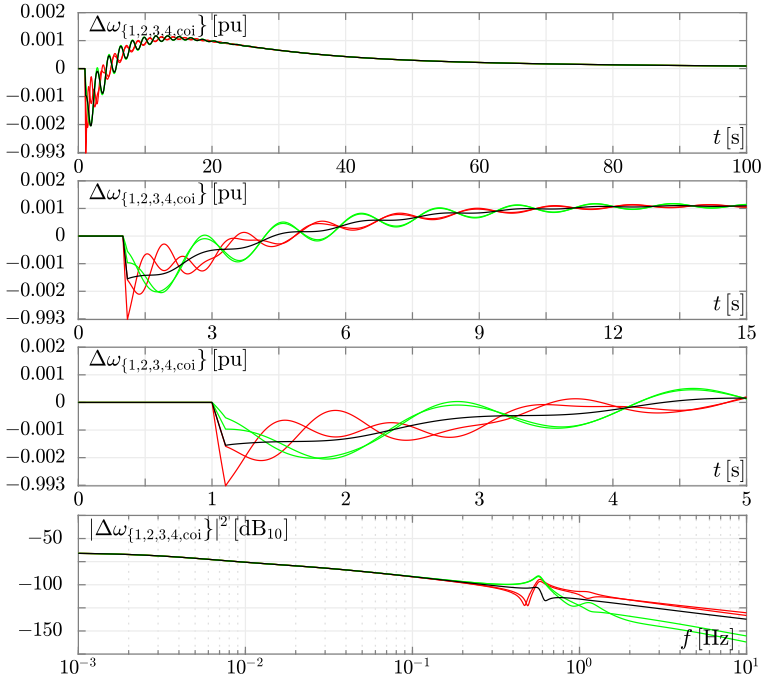

Fig. B.10. At $t = 1$ s, we applied a power imbalance in the Klein–Rogers–Kundur two-area system, by modifying the active and reactive power absorbed by the load connected at bus 7. This imbalance was removed after 0.1 s. The time evolution of the angular-speed deviation of the G_1 and G_2 generators in the Area 1 are reported in **red**, whereas the rotor speed deviation of the G_3 and G_4 generators in the Area 2 are reported in **green**. The $\Delta\omega_{\mathrm{coi}}$ angular-speed deviation of the center-of-inertia is shown in **black**. The same color code is adopted in the last panel for the frequency responses computed by applying a sinusoidal disturbance at bus 7 and sweeping frequency in [1 mHz, 10 Hz].

and it is possible to normalize $\boldsymbol{v}_1^{\mathrm{T}}$ in such a way that $\boldsymbol{v}_1^{\mathrm{T}}\boldsymbol{u}_1 = 1$ thus obtaining Eq. (5).

Appendix B

"How is it possible to reconcile the statement that *it is not possible to generally ensure that in properly connected power systems subject to random noise*, the components of $\Delta\boldsymbol{\omega}(t)$ share almost the same spectrum at low frequency?" To explain and support this statement, we would like to show some results concerning the Klein–Rogers–Kundur two-area, four machine system [44]. At $t = 1$ s, we applied a power imbalance by modifying the active and reactive power absorbed by the load connected at bus 7. This imbalance was removed after 0.1 s. The time evolution of the angular-speed deviations of the four generators are reported in the upper panel of Fig. B.10. It can be noticed that, after almost 30 s, the angular-speed deviation of the four generators evolve synchronously. This synchronization is expected and desired in properly connected and designed power systems as explained, for instance, in [22].

The $\Delta\omega_{\mathrm{COI}}$ angular-speed deviation of the center-of-inertia is shown in **black**. It can be noticed that, once the four generators evolve synchronously, their angular-speed deviations become identical to $\Delta\omega_{\mathrm{COI}}$.

In the second panel, we see the slow-coherence phenomenon as it is described in [63]. In particular, we can see relevant slow dynamics which are the low-frequency oscillations between coherent groups of stiffly connected machines (i.e., the ones in Area 1 and the ones in Area 2). In the third panel, we can observe the presence of *individual behaviors* for few seconds after the power imbalance removal, viz. fast dynamics which are the higher frequency oscillations between machines within the same individual coherent group. These three different types of evolution reflect in the frequency response computed by applying a sinusoidal disturbance at bus 7 and sweeping its frequency in the [1 mHz, 10 Hz] interval. The result of this frequency scan is reported in the last panel of Fig. B.10. We can observe that at "high" frequency the spectra of the angular-speed deviations are different, but at frequencies less than 0.7 Hz they start grouping in two groups and those in each group become closer and closer. The two groups become an ensemble at frequencies below almost 0.1 Hz. Then, for still lower frequency values, all the spectra almost perfectly overlap.

Note that, once the angular-speed deviations share almost the same spectrum, this spectrum is the one of the $\Delta\omega_{\mathrm{COI}}$ angular-speed deviation (**black** trace).

Appendix C

$$
\begin{aligned}
\Delta\omega(s) &= \frac{\mathbb{1}_{1,N}\boldsymbol{b}^{\mathrm{lf}}(s)}{s\mathcal{G}_{\mathcal{M}} + \mathbb{1}_{1,N}\left(\boldsymbol{D} + \left(s\boldsymbol{T}_g + \mathbb{1}_N\right)^{-1}\boldsymbol{k}_g\boldsymbol{R}^{-1}\right)\mathbb{1}_{N,1}} \underbrace{\sum_{j=1}^{N} b_j^{\mathrm{lf}}(s)}_{\eta(s)} \\
&= \frac{\eta(s)}{s\mathcal{G}_{\mathcal{M}} + \mathbb{1}_{1,N}\left(\mathrm{diag}\left(D_{11} + \frac{k_{g_{11}}}{R_{11}(sT_{g_{11}}+1)}, \ldots, D_{NN} + \frac{k_{g_{NN}}}{R_{NN}(sT_{g_{NN}}+1)}\right)\right)\mathbb{1}_{N,1}} \\
&= \frac{\eta(s)}{s\mathcal{G}_{\mathcal{M}} + \sum_{j=1}^{N} D_{jj} + \frac{k_{g_{jj}}}{R_{jj}\left(sT_{g_{jj}}+1\right)}} \\
&= \frac{\eta(s)}{s\mathcal{G}_{\mathcal{M}} + \sum_{j=1}^{N} D_{jj} + \frac{\frac{k_{g_{jj}}}{R_{jj}T_{g_{jj}}}}{s+\frac{1}{T_{g_{jj}}}}} \\
&= \frac{\eta(s)}{s\mathcal{G}_{\mathcal{M}} + \sum_{j=1}^{N} \frac{D_{jj}\left(s+\frac{1}{T_{g_{jj}}}\right)+\frac{k_{g_{jj}}}{R_{jj}T_{g_{jj}}}}{s+\frac{1}{T_{g_{jj}}}}}.
\end{aligned}
$$

Assuming that only $\widetilde{N} \leq N$ of the $T_{g_{jj}}$ constants are different, it is possible to define the $\{\widetilde{T}_{g_{ii}}\}$ set containing them and such that $\{\widetilde{T}_{g_{ii}}\} \subseteq$

$\{T_{g_{jj}}\}$. Hence,

$$\begin{aligned}\Delta\omega(s) &= \frac{\eta(s)\prod_{i=1}^{\widetilde{N}}\left(s+\frac{1}{\widetilde{T}_{g_{ii}}}\right)}{s^{\widetilde{N}+1}\mathcal{G}_{\mathcal{M}}+\sum_{i=0}^{\widetilde{N}} d_i s^i}\\ &= \frac{\eta(s)\left(\mathcal{G}_{\mathcal{M}}^{-1}s^{\widetilde{N}}+\sum_{i=0}^{\widetilde{N}-1} n_i s^i\right)}{s^{\widetilde{N}+1}+\sum_{i=0}^{\widetilde{N}} d_i s^i}\\ &= \eta(s)\sum_{k=1}^{\widetilde{N}+1}\frac{c_k}{s-a_k}\,.\end{aligned}$$

It is then easy to derive that $\mathcal{G}_{\mathcal{M}}^{-1}=\sum_{k=1}^{\widetilde{N}+1} c_k$

Appendix D

The coefficients that appear in Eq. (17) are:

$$\begin{aligned}\beta_3^1(s) &= \mathcal{M}_2 R_1 T_{g_1} b_1(s)\\ \beta_2^1(s) &= \left(\mathcal{D}_2 T_{g_1}+\mathcal{M}_2\right) R_1 b_1(s)\\ \beta_1^1(s) &= \left((b_1(s)\nu+b_2(s))T_{g_1}+\frac{b_1(s)\mathcal{D}_2}{\xi\Omega}\right)\xi\Omega R_1\\ \beta_0^1(s) &= \left(b_1(s)\nu+b_2(s)\right)\xi\Omega R_1\\ \beta_3^2(s) &= \mathcal{M}_2 R_1 T_{g_1} b_2(s)\\ \beta_2^2(s) &= \left(\mathcal{D}_1 T_{g_1}+\mathcal{M}_1\right) R_1 b_2(s)\\ \beta_1^2(s) &= \left((b_1(s)\nu+b_2(s))T_{g_1}+\frac{b_2(s)(\mathcal{D}_1+k_{g_1}R_1^{-1})}{\xi\Omega}\right)\xi\Omega R_1\\ \beta_0^2(s) &= \beta_0^1(s)\\ \alpha_4 &= \mathcal{M}_1\mathcal{M}_2 R_1 T_{g_1}\\ \alpha_3 &= R_1(T_{g_1}(\mathcal{D}_2\mathcal{M}_1+\mathcal{D}_1\mathcal{M}_2)+\mathcal{M}_1\mathcal{M}_2)\\ \alpha_2 &= \left(\frac{\mathcal{D}_2\left(\mathcal{D}_1 T_{g_1}+\mathcal{M}_1\right)+\mathcal{D}_1\mathcal{M}_2}{\xi\Omega}+\left(\mathcal{M}_1\nu+\mathcal{M}_2\right)T_{g_1}+\frac{k_1R_1^{-1}\mathcal{M}_2}{\xi\Omega}\right)\\ &\quad\times\xi\Omega R_1\\ \alpha_1 &= \left((\mathcal{D}_1\nu+\mathcal{D}_2)T_{g_1}+\mathcal{M}_1\nu+\mathcal{M}_2+\frac{\mathcal{D}_2\left(\mathcal{D}_1+k_{g_1}R_1^{-1}\right)}{\xi\Omega}\right)\xi\Omega R_1\\ \alpha_0 &= (\mathcal{D}_1\nu+\mathcal{D}_2+k_{g_1}R_1^{-1}\nu)\xi\Omega R_1\end{aligned}$$

References

[1] Tielens P, Van Hertem D. The relevance of inertia in power systems. Renew Sustain Energy Rev 2016;55:999–1009. http://dx.doi.org/10.1016/j.rser.2015.11.016, URL: https://www.sciencedirect.com/science/article/pii/S136403211501268X.

[2] Pierre JW, Zhou N, Tuffner FK, Hauer JF, Trudnowski DJ, Mittelstadt WA. Probing signal design for power system identification. IEEE Trans Power Syst 2010;25(2):835–43. http://dx.doi.org/10.1109/TPWRS.2009.2033801.

[3] Zhou N, Pierre J, Hauer J. Initial results in power system identification from injected probing signals using a subspace method. IEEE Trans Power Syst 2006;21(3):1296–302. http://dx.doi.org/10.1109/TPWRS.2006.879292.

[4] Chakraborty R, Jain H, Seo G-S. A review of active probing-based system identification techniques with applications in power systems. Int J Electr Power Energy Syst 2022;140:108008. http://dx.doi.org/10.1016/j.ijepes.2022.108008.

[5] Zhao J, Tang Y, Terzija V. Robust online estimation of power system center of inertia frequency. IEEE Trans Power Syst 2019;34(1):821–5.

[6] Ashton PM, Saunders CS, Taylor GA, Carter AM, Bradley ME. Inertia estimation of the GB power system using synchrophasor measurements. IEEE Trans Power Syst 2015;30(2):701–9.

[7] Gotti D, Ledesma P, Amaris H. A recursive system identification inertia estimator for traditional and converter-interfaced generators. Int J Electr Power Energy Syst 2023;154:109445. http://dx.doi.org/10.1016/j.ijepes.2023.109445, URL: https://www.sciencedirect.com/science/article/pii/S0142061523005021.

[8] del Giudice D, Grillo S. Analysis of the sensitivity of extended Kalman filter-based inertia estimation method to the assumed time of disturbance. Energies 2019;12(483).

[9] Wall P, Terzija V. Simultaneous estimation of the time of disturbance and inertia in power systems. IEEE Trans Power Deliv 2014;29(4):2018–31.

[10] Zeng F, Zhang J, Chen G, Wu Z, Huang S, Liang Y. Online estimation of power system inertia constant under normal operating conditions. IEEE Access 2020;8:101426–36.

[11] Baruzzi V, Lodi M, Oliveri A, Storace M. Analysis and improvement of an algorithm for the online inertia estimation in power grids with RES. In: 2021 IEEE international symposium on circuits and systems. ISCAS, 2021, p. 1–5. http://dx.doi.org/10.1109/ISCAS51556.2021.9401229.

[12] Bizzarri F, del Giudice D, Grillo S, Linaro D, Brambilla A, Milano F. Inertia estimation through covariance matrix. IEEE Trans Power Syst 2024;39(1):947–56. http://dx.doi.org/10.1109/TPWRS.2023.3236059.

[13] Shan Y, Wang Z, Wu J, Gao H. Evaluation of the inertia distribution performance for multi-machine power system. Int J Electr Power Energy Syst 2024;155:109595. http://dx.doi.org/10.1016/j.ijepes.2023.109595, URL: https://www.sciencedirect.com/science/article/pii/S014206152300652X.

[14] Allella F, Chiodo E, Giannuzzi GM, Lauria D, Mottola F. On-line estimation assessment of power systems inertia with high penetration of renewable generation. IEEE Access 2020;8:62689–97.

[15] Kontis EO, Pasiopoulou ID, Kirykos DA, Papadopoulos TA, Papagiannis GK. Estimation of power system inertia: A comparative assessment of measurement-based techniques. Electr Power Syst Res 2021;196:107250. http://dx.doi.org/10.1016/j.epsr.2021.107250.

[16] Dimoulias SC, Kontis EO, Papagiannis GK. Inertia estimation of synchronous devices: Review of available techniques and comparative assessment of conventional measurement-based approaches. Energies 2022;15(20):1–30.

[17] Prabhakar K, Jain SK, Padhy PK. Inertia estimation in modern power system: A comprehensive review. Electr Power Syst Res 2022;211:108222. http://dx.doi.org/10.1016/j.epsr.2022.108222.

[18] Hosaka N, Berry B, Miyazaki S. The world's first small power modulation injection approach for inertia estimation and demonstration in the island grid. In: 2019 8th international conference on renewable energy research and applications. ICRERA, 2019, p. 722–6. http://dx.doi.org/10.1109/ICRERA47325.2019.8997081.

[19] Tamrakar U, Guruwacharya N, Bhujel N, Wilches-Bernal F, Hansen TM, Tonkoski R. Inertia Estimation in Power Systems using Energy Storage and System Identification Techniques. In: 2020 international symposium on power electronics, electrical drives, automation and motion. SPEEDAM, 2020, p. 577–82. http://dx.doi.org/10.1109/SPEEDAM48782.2020.9161919.

[20] Rauniyar M, Berg S, Subedi S, Hansen TM, Fourney R, Tonkoski R, Tamrakar U. Evaluation of probing signals for implementing moving horizon inertia estimation in microgrids. In: 2020 52nd North American power symposium. NAPS 2020, 2021, http://dx.doi.org/10.1109/NAPS50074.2021.9449811.

[21] Zhang J, Xu H. Online identification of power system equivalent inertia constant. IEEE Trans Ind Electron 2017;64(10):8098–107. http://dx.doi.org/10.1109/TIE.2017.2698414.

[22] Sajadi A, Kenyon RW, Hodge B-M. Synchronization in electric power networks with inherent heterogeneity up to 100% inverter-based renewable generation. Nature Commun 2022;13(1). http://dx.doi.org/10.1038/s41467-022-30164-3.

[23] Rydin Gorjão L, Vanfretti L, Witthaut D, Beck C, Schäfer B. Phase and amplitude synchronization in power-grid frequency fluctuations in the nordic grid. IEEE Access 2022;10:18065–73. http://dx.doi.org/10.1109/ACCESS.2022.3150338.

[24] Guo Y, Zhang D, Li Z, Wang Q, Yu D. Overviews on the applications of the Kuramoto model in modern power system analysis. Int J Electr Power Energy Syst 2021;129. http://dx.doi.org/10.1016/j.ijepes.2021.106804.

[25] Zhu L, Hill DJ. Stability analysis of power systems: A network synchronization perspective. SIAM J Control Optim 2018;56(3):1640–64. http://dx.doi.org/10.1137/17M1118646.

[26] Nishikawa T, Molnar F, Motter AE. Stability landscape of power-grid synchronization. IFAC-PapersOnLine 2015;48(18):1–6. http://dx.doi.org/10.1016/j.ifacol.2015.11.001, 4th IFAC Conference on Analysis and Control of Chaotic Systems CHAOS 2015.

[27] Motter AE, Myers SA, Anghel M, Nishikawa T. Spontaneous synchrony in power-grid networks. Nat Phys 2013;9(3):191–7. http://dx.doi.org/10.1038/nphys2535.

[28] Ramaswamy G, Verghese G, Rouco L, Vialas C, DeMarco C. Synchrony, aggregation, and multi-area eigenanalysis. IEEE Trans Power Syst 1995;10(4):1986–93. http://dx.doi.org/10.1109/59.476067.

[29] Barać B, Krpan M, Capuder T, Kuzle I. Modeling and initialization of a virtual synchronous machine for power system fundamental frequency simulations. IEEE Access 2021;9:160116–34. http://dx.doi.org/10.1109/ACCESS.2021.3130375.

[30] Gustavsen B, Semlyen A. Rational approximation of frequency domain responses by vector fitting. IEEE Trans Power Deliv 1999;14(3):1052–61. http://dx.doi.org/10.1109/61.772353.

[31] Gustavsen B. Improving the pole relocating properties of vector fitting. IEEE Trans Power Deliv 2006;21(3):1587–92. http://dx.doi.org/10.1109/TPWRD.2005.860281.

[32] Triverio P. Vector fitting. In: Handbook on model order reduction. Berlin: De Gruyter; 2021, p. 275–310.
[33] Farkas M. Periodic motions. Springer-Verlag; 1994.
[34] Kuznetsov YA. Elements of applied bifurcation theory, 3rd ed.. Springer-Verlag; 2004.
[35] Demir A, Mehrotra A, Roychowdhury J. Phase noise in oscillators: a unifying theory and numerical methods for characterization. IEEE Trans Circuits Syst I 2000;47(5):655–74. http://dx.doi.org/10.1109/81.847872.
[36] Aulbach B. Continuous and discrete dynamics near manifolds of equilibria. Lecture notes in mathematics, Springer-Verlag; 1984.
[37] Sauer P, Pai MA. Power system steady-state stability and the load-flow Jacobian. IEEE Trans Power Syst 1990;5(4):1374–83.
[38] Machowski J, Lubosny Z, Bialek J, Bumby J. Power system dynamics: Stability and control. Wiley; 2020.
[39] Nwankpa C, Shahidehpour S. Colored noise modelling in the reliability evaluation of electric power systems. Appl Math Model 1990;14(7):338–51.
[40] Milano F, Zárate-Miñano R. A systematic method to model power systems as stochastic differential algebraic equations. IEEE Trans Power Syst 2013;28(4):4537–44. http://dx.doi.org/10.1109/TPWRS.2013.2266441.
[41] Hirpara RH, Sharma SN. An Ornstein–Uhlenbeck process-driven power system dynamics. IFAC-PapersOnLine 2015;48(30):409–14, 9th IFAC Symposium on Control of Power and Energy Systems CPES 2015.
[42] Roberts C, Stewart EM, Milano F. Validation of the ornstein-uhlenbeck process for load modeling based on μPMU measurements. In: 2016 power systems computation conference. PSCC, 2016, p. 1–7. http://dx.doi.org/10.1109/PSCC.2016.7540898.
[43] Abundo M. On the representation of an integrated Gauss–Markov process. Sci Math Jap Online E-2013 2013;719–23.
[44] Kundur P, Balu N, Lauby M. Power system stability and control. EPRI power system engineering series, McGraw-Hill; 1994.
[45] Pintelon R, Schoukens J. Design of excitation signals. In: System identification: a frequency domain approach. 2012, p. 151–75. http://dx.doi.org/10.1002/9781118287422.ch5.
[46] Boyd S. Multitone signals with low crest factor. IEEE Trans Circuits Syst 1986;33(10):1018–22.
[47] Friese M. Multitone signals with low crest factor. IEEE Trans Commun 1997;45(10):1338–44. http://dx.doi.org/10.1109/26.634697.
[48] Arnold L. Stochastic differential equations. A Wiley-interscience publication, Wiley; 1974.
[49] Hirpara RH, Sharma SN. An Ornstein–Uhlenbeck process-driven power system dynamics. IFAC-PapersOnLine 2015;48(30):409–14, 9th IFAC Symposium on Control of Power and Energy Systems CPES 2015.
[50] Nwankpa C, Shahidehpour S. Colored noise modelling in the reliability evaluation of electric power systems. Appl Math Model 1990;14(7):338–51.
[51] Gillespie DT. Exact numerical simulation of the Ornstein-Uhlenbeck process and its integral. Phys Rev E 1996;54:2084–91. http://dx.doi.org/10.1103/PhysRevE.54.2084.
[52] Milshtein GN, Tret'yakov MV. Numerical solution of differential equations with colored noise. J Stat Phys 1994;77(3):691–715. http://dx.doi.org/10.1007/BF02179457.
[53] Bizzarri F, Brambilla A, Storti Gajani G, Banerjee S. Simulation of real world circuits: Extending conventional analysis methods to circuits described by heterogeneous languages. IEEE Circuits Syst Mag 2014;14(4):51–70.
[54] Bizzarri F, Brambilla A. PAN and MPanSuite: Simulation vehicles towards the analysis and design of heterogeneous mixed electrical systems. In: NGCAS, Genova, Italy. 2017, p. 1–4.
[55] Linaro D, del Giudice D, Bizzarri F, Brambilla A. PanSuite: A free simulation environment for the analysis of hybrid electrical power systems. Electr Power Syst Res 2022;212.
[56] Athay T, Podmore R, Virmani S. A practical method for the direct analysis of transient stability. IEEE Trans Power Appl Syst 1979;PAS-98(2):573–84. http://dx.doi.org/10.1109/TPAS.1979.319407.
[57] Zimmerman RD, Murillo-Sánchez CE, Thomas RJ. MATPOWER: Steady-state operations, planning, and analysis tools for power systems research and education. IEEE Trans Power Syst 2010;26(1):12–9.
[58] Energy Development and Power Generation Committee. IEEE recommended practice for excitation system models for power system stability studies. IEEE std 421.5-2016 (revision of IEEE std 421.5-2005), 2016, p. 1–207. http://dx.doi.org/10.1109/IEEESTD.2016.7553421.
[59] Gotti D, Bizzarri F, Brambilla A, Giudice Dd, Grillo S, Linaro D, Ledesma P, Amaris H. Inertia estimation of a Power System Area based on iterative equation error system identification. IEEE Trans Power Syst 2024;1–13. http://dx.doi.org/10.1109/TPWRS.2024.3353077.
[60] Wilson D, Yu J, Al-Ashwal N, Heimisson B, Terzija V. Measuring effective area inertia to determine fast-acting frequency response requirements. Int J Electr Power Energy Syst 2019;113:1–8. http://dx.doi.org/10.1016/j.ijepes.2019.05.034, URL: https://www.sciencedirect.com/science/article/pii/S0142061519304892.
[61] Linaro D, Bizzarri F, del Giudice D, Pisani C, Giannuzzi C, Grillo S, Brambilla AM. Continuous estimation of power system inertia using convolutional neural networks. Nature Commun 2023;14(1). http://dx.doi.org/10.1038/s41467-023-40192-2.
[62] Poolla BK, Bolognani S, Dörfler F. Optimal placement of virtual inertia in power grids. IEEE Trans Autom Control 2017;62(12):6209–20. http://dx.doi.org/10.1109/TAC.2017.2703302.
[63] Chow JH. Slow coherency and aggregation. In: Chow JH, editor. Power system coherency and model reduction. New York, NY: Springer New York; 2013, p. 39–72. http://dx.doi.org/10.1007/978-1-4614-1803-0_3.